



# David Taylor Research Center

Bethesda, MD 20084-5000

DTRC/SHD-1003-06 August 1991

Ship Hydromechanics Department

Departmental Report

DTIC  
DEC 3 1991  
C

COMPUTATION OF THE HYDRODYNAMIC FORCES AND MOMENTS ON  
A BODY OF REVOLUTION WITH AND WITHOUT APPENDAGES

by

Young S. Hong

Approved for public release.

Distribution is unlimited.



91-16999



## MAJOR DTRC TECHNICAL COMPONENTS

CODE 011 DIRECTOR OF TECHNOLOGY, PLANS AND ASSESSMENT

12 SHIP SYSTEMS INTEGRATION DEPARTMENT

14 SHIP ELECTROMAGNETIC SIGNATURES DEPARTMENT

15 SHIP HYDROMECHANICS DEPARTMENT

16 AVIATION DEPARTMENT

17 SHIP STRUCTURES AND PROTECTION DEPARTMENT

18 COMPUTATION, MATHEMATICS & LOGISTICS DEPARTMENT

19 SHIP ACOUSTICS DEPARTMENT

27 PROPULSION AND AUXILIARY SYSTEMS DEPARTMENT

28 SHIP MATERIALS ENGINEERING DEPARTMENT

### DTRC ISSUES THREE TYPES OF REPORTS:

1. **DTRC reports, a formal series**, contain information of permanent technical value. They carry a consecutive numerical identification regardless of their classification or the originating department.
2. **Departmental reports, a semiformal series**, contain information of a preliminary, temporary, or proprietary nature or of limited interest or significance. They carry a departmental alphanumeric identification.
3. **Technical memoranda, an informal series**, contain technical documentation of limited use and interest. They are primarily working papers intended for internal use. They carry an identifying number which indicates their type and the numerical code of the originating department. Any distribution outside DTRC must be approved by the head of the originating department on a case-by-case basis.

## REPORT DOCUMENTATION PAGE

1a. REPORT SECURITY CLASSIFICATION Unclassified		1b. RESTRICTIVE MARKINGS	
2a. SECURITY CLASSIFICATION AUTHORITY		3 DISTRIBUTION/AVAILABILITY OF REPORT Approved for public release. Distribution is unlimited.	
2b. DECLASSIFICATION/DOWNGRADING SCHEDULE		5 MONITORING ORGANIZATION REPORT NUMBER(S)	
4. PERFORMING ORGANIZATION REPORT NUMBER(S) DTRC/SHD-1003-06		7a. NAME OF MONITORING ORGANIZATION	
6a. NAME OF PERFORMING ORGANIZATION David Taylor Research Center	6b. OFFICE SYMBOL (if applicable) 1564	7b. ADDRESS (City, State, and ZIP Code)	
6c. ADDRESS (City, State, and ZIP Code) Bethesda, MD 20084-5000		9 PROCUREMENT INSTRUMENT IDENTIFICATION NUMBER	
8a. NAME OF FUNDING/SPONSORING ORGANIZATION DARPA	8b. OFFICE SYMBOL (if applicable)	10 SOURCE OF FUNDING NUMBERS	
8c. ADDRESS (City, State, and ZIP Code) 1515 Wilson Blvd., Suite 705 Arlington, VA 22209		PROGRAM ELEMENT NO 63569N	PROJECT NO none
		TASK NO. none	WORK UNIT ACCESSION NO. DN 509067
11 TITLE (Include Security Classification) Computation of the Hydrodynamic Forces and Moments on a Body of Revolution with and without Appendages			
12 PERSONAL AUTHOR(S) Y. Hong			
13a. TYPE OF REPORT Departmental	13b. TIME COVERED FROM _____ TO _____	14 DATE OF REPORT (Year, Month, Day) August 1991	15 PAGE COUNT
16 SUPPLEMENTARY NOTATION			
17 COSATI CODES		18 SUBJECT TERMS (Continue on reverse if necessary and identify by block number)	
FIELD	GROUP	SUB-GROUP	
		Submarine Hydrodynamic Stability	
		Control Potential Flow Separation	
19 ABSTRACT (Continue on reverse if necessary and identify by block number)			
<p>An analytical method was developed to predict the hydrodynamic forces and moments developed on a body of revolution with and without appendages. The appendages included a bridge fairwater, sternplanes, and rudders. It was assumed that the body was either translating with an angle of attack of up to 20 degrees or rotating with an angular velocity. Calculations were performed by using the analytical method for four different bodies of revolution and comparisons were made with available experimental data. Potential flow was used to determine the inviscid contribution to the hydrodynamic forces and moments.</p> <p>[continued on back]</p>			
20 DISTRIBUTION/AVAILABILITY OF ABSTRACT <input type="checkbox"/> UNCLASSIFIED/UNLIMITED <input type="checkbox"/> SAME AS RPT <input type="checkbox"/> DTIC USERS		21 ABSTRACT SECURITY CLASSIFICATION Unclassified	
22a. NAME OF RESPONSIBLE INDIVIDUAL J. Feldman		22b. TELEPHONE (Include Area Code) 301-227-1475	22c. OFFICE SYMBOL 1564

## 19. [continued]

The viscous contribution to the hydrodynamic forces and moments was determined by assuming that there was no flow separation due to the axial flow, and that the flow separation on the leeward side of the body due to the crossflow was independent of the offsets of the body, the angle of attack, the angular velocity, and the forward speed. It was assumed that the angle at which the flow separates, as measured from the stagnation point, was 110 degrees at the stern and 170 degrees at the bow for the body at angle of attack and 160 degrees for the body with an angular velocity.

## CONTENTS

page

NOTATIONS .....	v
ABSTRACT .....	1
ADMINISTRATIVE INFORMATION .....	1
INTRODUCTION .....	1
INVISCID FORCE COMPUTATION .....	2
VISCOUS FORCE COMPUTATION .....	4
CORRECTION TO AXIAL VELOCITY .....	7
TANGENTIAL VELOCITY IN THE CROSSFLOW DIRECTION .....	7
FORCE COMPUTATION FOR THE CONTROL SURFACES .....	8
LIFT COMPUTATION FOR TWO-DIMENSIONAL WING SECTIONS .....	9
INTERACTION EFFECT BETWEEN BODY AND CONTROL SURFACES .....	11
DISCUSSION OF NUMERICAL RESULTS .....	12
TWO-DIMENSIONAL SEPARATION ANGLES IN CROSSFLOW	
DIRECTION .....	12
GEOMETRIC CHARACTERISTICS OF THE CONFIGURATIONS .....	13
RESULTS OF THE CALCULATIONS FOR THE UNAPPENDED HULL .....	13
RESULTS OF THE CALCULATIONS FOR THE CONTROL SURFACES .....	14
RESULTS OF THE CALCULATIONS FOR THE PARTIALLY	
APPENDED BODY .....	14
UNCERTAINTY ANALYSIS FOR THE NUMERICAL PROCEDURES .....	15
CONCLUSIONS .....	15
RECOMMENDATIONS .....	16
ACKNOWLEDGMENTS .....	16
REFERENCES .....	47

## FIGURES

1. Coordinate system for the straightline motion .....	17
2. Coordinate system for the rotational motion .....	18
3. Axial velocity of the Akron airship when $\alpha = 0$ degree .....	19
4. Tangential velocity of Model 4621 in the crossflow	
direction when $\alpha = 12$ degrees .....	20
5. Tangential velocity of Model 4621 in the crossflow	
direction when $\beta = 5$ degrees and $r' = 0.389$ .....	21
6. Coordinate system for a finite wing .....	22
7. Sectional contour of a finite wing .....	23
8. Measured separation angles of a spheroid when $\alpha = 30$	
degrees .....	24
9. Axial forces of Series 58 when $\alpha = 0$ degree .....	25
10. Forces and moments of a spheroid with $L/D=4$ for	
straightline motion .....	26
11. Forces and moments of the Akron airship for	
straightline motion .....	27

12. Forces and moments of Model 4621 for straightline motion .....	28
13. Forces and moments of the DARPA SUBOFF for straightline motion .....	29
14. Forces and moments of a spheroid with $L/D=4$ for rotational motion with $r' = -0.072$ .....	30
15. Forces and moments of Model 4621 for rotational motion .....	31
16. Forces and moments of a finite wing with an NACA 0015 section shape .....	34
17. Geometric characteristics of the appendages .....	37
18. Forces and moments of Model 4621 with appendages for straightline motion .....	38
19. Forces and moments of the DARPA SUBOFF with bridge fairwater for straightline motion .....	41
20. Forces and moments of the DARPA SUBOFF with stern appendages for straightline motion .....	42
21. Forces and moments of Model 4621 with Appendage 3C for rotational motion .....	43

#### TABLES

1. Geometric characteristics of sample models .....	46
2. Estimated errors in the numerical procedures performed for the Akron airship .....	46

# NOTATIONS

A	Aspect ratio of a finite wing = $b/c_m$
b	Span of a finite wing
$C_A$	Total drag in the axial direction
$c_m$	Mean chord of a finite wing
$C_{Di}$	Induced drag
$C_p$	Pressure coefficient
D	Beam or Diameter
$D_F$	Frictional Drag
$D_p$	Form Drag
$F_X = \rho L^2 U_o^2 C_X / 2$	Axial force in the OX-axis
$F_Z = \rho L^2 U_o^2 C_Z / 2$	Normal force in the OZ-axis
$F_U = \rho L^2 U_o^2 C_U / 2$	Force parallel to $U_o$
$F_L = \rho L^2 U_o^2 C_L / 2$	Force normal to $U_o$ or lift
L	Length of body
$M_Y = \rho L^3 U_o^2 C_{M_Y} / 2$	Pitch moment about C.G.
g	Gravitational acceleration
H	Distance between the free surface and C.G.
p	Pressure
$r'$	Turning rate
$Re = U_o L / \nu$	Reynolds number
$U_o$	Velocity of the body
$U_1 = U_o \cos \alpha$ or $U_o \cos \beta$	Free stream velocity in the OX-axis
$U_2 = U_o \sin \alpha$ or $U_o \sin \beta$	Free stream velocity in the OZ-axis
$U_{sp}$	Velocity at two-dimensional separation
$\nu$	Viscosity of the fluid
$\alpha$	Angle of attack
$\beta$	Drift angle
$\gamma$	Two-dimensional vortex strength
$\Omega$	Angular velocity of body
$\rho$	Fluid density
$\kappa$	Momentum area
$\delta$	Boundary layer thickness
$\tau$	Skin friction
$\theta_{sp}$	Angle of two-dimensional separation

Accession For	
DTIC UNCLASS	<input checked="" type="checkbox"/>
DTIC TAB	<input type="checkbox"/>
Unannounced	<input type="checkbox"/>
Justification	
By	
Distribution/	
Availability Codes	
Dist	Avail and/or Special
A-1	



## ABSTRACT

An analytical method was developed to predict the hydrodynamic forces and moments developed on a body of revolution with and without appendages. The appendages included a bridge fairwater, sternplanes, and rudders. It was assumed that the body was either translating with an angle of attack of up to 20 degrees or rotating with an angular velocity. Calculations were performed by using the analytical method for four different bodies of revolutions and comparisons were made with available experimental data. Potential flow was used to determine the inviscid contribution to the hydrodynamic forces and moments. The viscous contribution to the hydrodynamic forces and moments was determined by assuming that there was no flow separation due to the axial flow, and that the flow separation on the leeward side of body due to the crossflow was independent of the offsets of the body, the angle of attack, the angular velocity, and the forward speed. It was assumed that the angle at which the flow separates, as measured from the stagnation point, was 110 degrees at the stern and 170 degrees at the bow for the body at angle of attack and 160 degrees for the body with an angular velocity.

## ADMINISTRATIVE INFORMATION

This work was sponsored by the Submarine Technology Program (STP) Office of the Defense Advanced Research Projects Agency (DARPA) under Task Area S1974-030, Program Element 63569N. The David Taylor Research Center Work Unit Number was 1540-002.

## INTRODUCTION

The accurate prediction of the hydrodynamic forces and moments developed on the hull and appendages of a submerged vehicle is required for determining its stability, control, and maneuvering characteristics. Various analytical methods have been developed to make these predictions, including those of computational fluid dynamics, but none of them have been successful at the present time. This is because it is particularly difficult to accurately determine both the distribution of the velocity over the surface of the hull and the location of the separation lines. A limited amount of experimental data exist for various bodies of revolution at zero angle of attack and for a spheroid at small angles of attack.

When a streamlined body of revolution is moving through the fluid with an angle of attack, the flow separates from the hull. The location of the lines of separation has an important effect on the magnitudes of the hydrodynamic forces and moments developed on the hull. For example, once there is flow separation, the form (pressure) drag becomes much larger than the frictional drag.



Computational fluid dynamics can be used to solve the Navier-Stokes equations and, hence, calculate the velocity distribution for the flow around a body of revolution at small angles of attack. However, at the present time there are no validated methods for determining the location of the separation lines. Due to the difficulty of using computational fluid dynamics for calculating the location of the separation lines, an approximate method has been developed to compute the hydrodynamic forces and moments for a submerged vehicle.

As discussed in Reference 1, the method assumes that the total hydrodynamic force and moment can be divided into inviscid and viscous contributions. Inviscid flow is assumed for determining the velocity and pressure distributions over a particular cross section of the hull from the stagnation point on the windward side to the point where the flow separates. After the flow separates on the leeward side, the pressure is assumed to be constant.

The location of the two-dimensional crossflow lines of separation is determined empirically. The angular location is measured from the windward stagnation point. For straightline motion, the angle is selected to be 170 degrees at the bow and 110 degrees at the stern.

The viscous contribution to the hydrodynamic forces and moments is determined by solving the two-dimensional boundary layer equation for a body of revolution. It is assumed that there is no flow separation in the axial direction. The forces on the control surfaces are computed using lifting line theory.

This report describes the method for calculating the inviscid and viscous contributions to the hydrodynamic forces and moments on the hull, describes the method for calculating the forces on the control surfaces, and discusses the results of the calculations.

#### INVISCID FORCE COMPUTATION

The coordinate system,  $oxyz$  moves at a speed of  $U_0$ , which is the mean speed of the body along the positive  $ox$ -axis (see Figure 1) for the straightline motion. The positive  $oz$ -axis is always directed vertically upwards. The origin,  $o$  or  $O$  is located at the center of gravity of the body. The  $Ox$ -axis is parallel to the body axis and the  $Oz$ -axis is perpendicular to the body axis. When the body is undergoing a rotational motion, a positive drift angle is defined as shown in Figure 1.

The total velocity potential can be expressed as

$$\Phi(x,y,z) = \Phi_0(x,y,z) + \phi(x,y,z) \quad (1)$$

where  $\phi$  is disturbance velocity potential due to the body. The gradient of  $\Phi_0$  is given as

$$\begin{aligned} \nabla\Phi_0 &= (-U_0, 0, 0), & \text{for straightline motion} \\ &= (R\Omega - y, \Omega x, 0), & \text{for rotational motion} \end{aligned} \quad (2)$$

The disturbance velocity potential  $\phi$  can be expressed in the integral form as

$$\phi(x, y, z) = \frac{1}{4\pi} \iint_S G(P, Q) \sigma(Q) dS(Q) \quad (3)$$

where  $P(x, y, z)$  is the field point,  $Q(x_0, y_0, z_0)$  the source point,  $S$  the body surface,  $\sigma$  the unknown strength of sources and sinks distributed on the body surface, and  $G$  is the Green function which is given as

$$G(P, Q) = \frac{1}{r} \quad (4)$$

where

$$r^2 = (x-x_0)^2 + (y-y_0)^2 + (z-z_0)^2 \quad (5)$$

The unknown strength of sources and sinks,  $\sigma$  is determined by the body boundary condition which is

$$\frac{\partial}{\partial n} \left\{ \frac{1}{4\pi} \iint_S G(P, Q) \sigma(Q) dS(Q) \right\} = -\nabla \phi_0 \cdot \vec{n} \quad (6)$$

The forces acting on the body is expressed as

$$\vec{F} = - \iint_S p \vec{n} dS \quad (7)$$

where  $\vec{n}$  is the unit normal vector at the body surface and  $p$ , the pressure around the body, is

$$p = \frac{\rho}{2} [|\nabla \phi|^2 - |\nabla \phi_0|^2] \quad (8)$$

where  $\rho$  is the density of the fluid. The detailed procedure of the numerical solution of Equation (6) is given in Reference 2. The body surface is discretized with many surface elements. The unknown strengths of sources and sinks are assumed constant on each surface element. Then, Equation (6) can be expressed as

$$\frac{1}{4\pi} \sum_{i=1}^N \sigma_i \iint_{S_i} \frac{\partial}{\partial n} \left( \frac{1}{r} \right) dS = - \left( \frac{\partial \phi_0}{\partial n} \right)_i \quad (9)$$

When the kernel integral is numerically evaluated, the solution of Equation (9) is same as that of system of linear equations.

# VISCOUS FORCE COMPUTATION

For the computation of the axial force which is parallel to the OX-axis the method developed by Young (Reference 3) is used. In this method it is assumed there is no separation in the flow.

The total drag coefficient is expressed as

$$C_A = \frac{2\kappa_0}{S} = \frac{2\kappa_t}{S} \left( \frac{U_t}{U_1} \right)^{3.2} \quad (10)$$

where S is the surface area of the body. The momentum area of the wake far downstream is defined as

$$\kappa_0 = 2\pi \int_0^\infty \frac{u}{U_1} \left( 1 - \frac{u}{U_1} \right) y dy \quad (11)$$

where u is the velocity in the wake parallel to the body axis and  $U_1$  the incoming velocity parallel to the body axis. The velocity  $U_1$  can be expressed as

$$\begin{aligned} U_1 &= U_0 \cos \alpha, & \text{for motion in the vertical plane} \\ &= U_0 \cos \beta, & \text{for motion in the horizontal plane} \\ &= R\Omega \cos \beta, & \text{for rotational motion} \end{aligned} \quad (12)$$

In Equation (10)  $\kappa_t$  is the momentum area at the tail and  $U_t$  the velocity at the edge of the boundary layer at the tail. In order to compute  $\kappa_t$ , the laminar boundary layer equation of a body of revolution is solved up to the transition point and then, the turbulent boundary layer is computed up to the tail. The laminar boundary layer equation is expressed with an assumed velocity equation in the boundary layer as

$$\frac{dz}{dx} = \frac{f(\lambda)}{U} - \left( \frac{r'}{r} \frac{U}{U'} \right) \frac{f^*(\lambda)}{U} + z^2 U'^{1/2} g(\lambda) \quad (13)$$

where

$$z = \delta^2/\nu$$

$$\lambda = U'z = z\left(\frac{dU}{dx}\right)$$

$$f(\lambda) = (4 - \frac{232}{315}\lambda + \frac{79}{3780}\lambda^2 + \frac{2}{4536}\lambda^3)/C$$

$$f^*(\lambda) = (\frac{74}{315}\lambda - \frac{2}{945}\lambda^2 - \frac{\lambda^3}{4536})/C \quad (14)$$

$$g(\lambda) = (\frac{2}{945} + \frac{\lambda}{2268})/C$$

$$C = \frac{37}{315} - \frac{\lambda}{315} - \frac{5}{9072}\lambda^2$$

In Equation (13),  $x$  is the distance measured along the surface of the body from the stagnation point,  $r$  is the radius of the body,  $\delta$  is the boundary layer thickness,  $U$  is the velocity at the edge of the boundary layer, and  $\nu$  is the kinematic viscosity of the fluid. The equation of the momentum area for the turbulent layer is expressed as

$$\frac{d\kappa}{dx} + \frac{U'}{U}(H + 2)\kappa = \frac{\tau_o}{\rho U^2} 2\pi r \quad (15)$$

where  $H(=1.4)$  is the ratio of displacement thickness to momentum area and  $\tau_o$  is the skin friction at the body surface. When Equation (15) is solved up to the tail, the total drag can be computed using Equation (10). The details of the derivation of Equations (13) through (15) are given in References 3 and 4.

The method to compute normal force and its moment is slightly different from that to compute axial force. The sectional crossflow drag is integrated along the axis of the body. The two-dimensional flow is given by

$$U = 2U_2 \sin\theta \quad (16)$$

where  $U_2$  is the two-dimensional free stream velocity (see Figure 2). The velocity  $U_2$  can be expressed as

$$\begin{aligned} U_2 &= U_o \sin\alpha, \quad \text{for motion in the vertical plane} \\ &= U_o \sin\beta, \quad \text{for motion in the horizontal plane} \\ &= \Omega y, \quad \text{for rotational motion} \end{aligned} \quad (17)$$

Furthermore, it is assumed that the flow separates and the separation point must be known to perform the computation. The crossflow drag is expressed as

$$D_{2D} = D_F + D_P \quad (18)$$

where  $D_F$  is the frictional drag and  $D_P$  is the form drag.

For a two-dimensional section, the laminar boundary layer equation becomes

$$\frac{dz}{dx} = \frac{f(\lambda)}{U} + z^2 U'' g(\lambda) \quad (19)$$

and the skin friction is given by (see Reference 3)

$$\tau_o = \frac{\rho \nu (\lambda + 12) U}{6 \delta} \quad (20)$$

The turbulent boundary layer equation is the same as Equation (15) with omission of  $2\pi r$  on the right-hand side. The frictional drag can be computed by the integration of skin friction  $\tau_o$  along the body axis after Equations (15), (19), and (20) are solved numerically.

The pressure in the separated region is assumed constant and the pressure coefficient is expressed as

$$\begin{aligned} C_p &= 1 - \left(\frac{U}{U_2}\right)^2, \text{ when } \theta < \theta_{sp} \\ &= 1 - \left(\frac{U_{sp}}{U_2}\right)^2, \text{ when } \theta > \theta_{sp} \end{aligned} \quad (21)$$

where  $U_{sp}$  is the velocity at the point of separation. Then the form drag is computed as follows:

$$D_P = \rho U_2^2 \int_0^\pi C_p r \cos \theta \, d\theta \quad (22)$$

where  $\theta_{sp}$  is the angle at the point of separation as shown in Figure 2. The velocity  $U$  in Equations (13) and (19) is the tangential velocity in the axial and crossflow direction, respectively. Even though the tangential velocity in the crossflow direction is simply expressed with Equation (17), this velocity is computed around the body section with application of potential theory as described in the previous section.

### CORRECTION TO AXIAL VELOCITY

The velocity distribution on the body surface can be computed by differentiating Equation (1) with respect to  $x$ ,  $y$ , and  $z$  as

$$\vec{V} = (u, v, w) = \nabla(\phi_0 + \phi) \quad (23)$$

The tangential velocity on the body surface in the axial direction is

$$U = \vec{V} \cdot \vec{t}_1 \quad (24)$$

where  $\vec{t}_1$  is the unit tangential vector in the axial direction and it can be expressed as

$$\vec{t}_1 = \vec{t}_2 \times \vec{n} \quad (25)$$

where  $\vec{t}_2$  is the unit tangential vector in the crossflow direction and given in Equation (27). The velocity of the airship Akron expressed with Equation (24) is plotted in Figure 3. The computed velocity agrees very well with the measured velocity up to 95% of the body length. This velocity becomes zero at the stern. However, the measured velocity shown in Reference 5 does not become zero at the stern. In order to make the computed velocity close to the measured one, the velocities near the stern are extrapolated as shown in Figure 3. The extrapolated velocity distribution agrees well with the measured velocity. The extrapolation scheme for the velocity at the stern was adopted by Cebeci and Smith for the solution of three-dimensional boundary layer equations (Reference 6).

### TANGENTIAL VELOCITY IN THE CROSSFLOW DIRECTION

The tangential velocity in the crossflow direction can be expressed as

$$U = \vec{V} \cdot \vec{t}_2 \quad (26)$$

where  $\vec{t}_2$  is the unit tangential vector in the crossflow direction and it can be expressed as

$$\begin{aligned}\vec{t}_2 &= (\cos\theta\sin\alpha, \sin\theta, \cos\theta\cos\alpha) \text{ or} \\ &= (\sin\theta\sin\beta, \sin\theta\cos\beta, -\cos\theta) \text{ with } \theta = \tan^{-1}(Z/Y)\end{aligned}\quad (27)$$

The computed tangential velocity in the crossflow direction for the straight-line motion is plotted in Figure 4 and it is compared with Equation (16). The agreement is very good. This indicates that for the straightline motion the tangential velocity in the crossflow direction can be computed with Equation (16). The direction of the flow is always in one direction. The computed tangential velocity in the crossflow direction for the rotational motion is plotted in Figure 5. Compared with the results of Equation (16), the computed velocity does not agree well. Furthermore, there is change in flow direction depending on the location of the section. The location of the maximum velocity is always 90 degrees from the horizontal plane.

#### FORCE COMPUTATION FOR THE CONTROL SURFACES

To compute forces and moments of the control surfaces, the method which has been developed for the airplane wing by Sivells and Neely (Reference 7) are used herein. In this method the distributed lift along the wing span is computed with the lifting line theory. The sectional lift is computed at the effective angle of attack which can be expressed as

$$\alpha_e = \alpha_o - \alpha_i \quad (28)$$

where  $\alpha_o$  is the geometric angle of attack and  $\alpha_i$  the induced angle of attack (see Figure 6).

To compute the induced angle of attack, the half span of the control plane is divided as follows

$$y = \frac{b}{2} \cos\theta, \quad \theta = 9, 18, \dots, 81, 90 \quad (29)$$

When  $\theta$  is 0, the section is located at the tip and when  $\theta$  is 90, the section is located at the midspan.

The sectional lift is approximated as

$$C_l(y) = \frac{A}{A+1.8} \left\{ 0.5 + \frac{2C_m}{\pi c_i} \left[ 1 - \left( \frac{2y}{b} \right)^2 \right]^{\frac{1}{2}} \right\} C_l(\alpha_o) \quad (30)$$

where  $A (=b/c_o)$  is the aspect ratio,  $c_m$  is the mean chord,  $c_i$  is the chord at  $y$ , and  $C_l(\alpha_o)$  is the two-dimensional lift coefficient for  $\alpha_o$ . The induced angle of attack is expressed as

$$\alpha_i = \frac{\int \frac{d[c_l(y)]}{y_i - y}}{U_o} \quad (31)$$

Once the induced angle of attack is known, the induced drag is computed as

$$C_{Di} = C_l \tan \alpha_i \quad (32)$$

At the tip of the control surface, the induced angle of attack is set equal to the geometric angle of attack if the induced angle of attack is calculated, using Equation (31), to be larger than the geometric angle of attack. Since the calculated sectional lift is smaller than the experimental lift, a correlation factor of 0.8 is applied to Equation (31).

#### LIFT COMPUTATION FOR THE TWO-DIMENSIONAL WING SECTIONS

The forces on a two-dimensional wing section can be computed with the vortex panel method described in Reference 8. The sectional contour is replaced with a two-dimensional vortex singularity and the strength of this singularity is determined by the body boundary condition that the normal velocity at the body is zero. The sectional contour is discretized with  $m$  straight segments as shown in Figure 7. The strength of vortex singularity varies linearly on each segment. The velocity potential at the  $i$ th control point  $(x_i, y_i)$  can be expressed as

$$\psi(x_i, y_i) = U_o x_i - \sum_{j=1}^m \int \frac{\gamma(s_j)}{2\pi} \tan^{-1} \left( \frac{y_i - y_j}{x_i - x_j} \right) ds_j \quad (33)$$

where  $\gamma(s_j)$  is the strength of vortex singularity at the  $j$ th segment which can be expressed as

$$\gamma(s_j) = \gamma_j + (\gamma_{j+1} - \gamma_j) \frac{s_j}{S_j} \quad (34)$$

$S_j$  in Equation (34) represents the length of the  $j$ th segment, and  $\gamma_j$  and  $\gamma_{j+1}$  are the vortex strengths at the beginning and at the end of the  $j$ th segment, respectively. The  $(m+1)$  values of  $\gamma_j$  at boundary points  $(X_j, Y_j)$  are unknown constants to be determined numerically. The boundary condition of no flow through the wing requires that the velocity in the direction of the outward normal vector be vanishing at the  $i$ th control point, so that

$$\frac{\partial}{\partial n} \psi(x_i, y_i) = 0, \text{ for } i=1, 2, \dots, m \quad (35)$$



The unit normal vector is expressed as

$$\vec{n}_i = (-\sin\theta_i, \cos\theta_i) \quad (36)$$

If we carry out the involved differentiation and integration along the segments, we obtain the followings

$$\sum_{j=1}^m (C_{n1}\gamma_j + C_{n2}\gamma_{j+1}) = 2\pi U_0 \sin\theta_i, \text{ for } i=1, 2, \dots, m \quad (37)$$

where

$$\begin{aligned} C_{n1} &= 0.5FD + CG - C_{n2} \\ C_{n2} &= D + FQ/(2S_j) - G(AC + DE)/S_j \\ A &= -[(x_i - x_j)\cos\theta_j + (y_i - y_j)\sin\theta_j] \\ B &= (x_i - x_j)^2 + (y_i - y_j)^2 \\ C &= \sin(\theta_i - \theta_j) \\ D &= \cos(\theta_i - \theta_j) \\ E &= (x_i - x_j)\sin\theta_j - (y_i - y_j)\cos\theta_j \\ F &= \ln(1 + \frac{S_j^2 + 2AS_j}{B}) \\ G &= \tan^{-1}(\frac{ES_j}{B + AS_j}) \\ P &= (x_i - x_j)\sin(\theta_i - 2\theta_j) + (y_i - y_j)\cos(\theta_i - 2\theta_j) \\ Q &= (x_i - x_j)\cos(\theta_i - 2\theta_j) - (y_i - y_j)\sin(\theta_i - 2\theta_j) \end{aligned} \quad (38)$$

When  $i=j$ , the coefficients,  $C$ ,  $E$ , and  $F$  become zero; and  $C_{n1}$  and  $C_{n2}$  in Equation (38) have simplified values as follows

$$C_{n1} = -1 \quad (39)$$

$$C_{n2} = 1$$

Since all of the coefficients in Equation (38) are dependent on the shape of the sectional contour, the coefficients  $C_{n1}$  and  $C_{n2}$  can be evaluated easily. Once  $C_{n1}$  and  $C_{n2}$  are numerically evaluated, the unknown strengths of vortex,  $\gamma_i$ , can be solved using Equation (37). However, there are only  $m$  equations in Equation (37) for  $(m+1)$  unknowns. The last equation which supplements Equation (37) can be obtained with the Kutta condition that the strength of vortex at the trailing edge be zero as follows

$$\gamma_1 + \gamma_{m+1} = 0 \quad (40)$$

Once the vortex strengths are numerically solved, the velocity components can be computed through differentiation of Equation (33) with respect to  $x_i$  and  $y_i$ . The pressure on the contour is given as

$$p = \frac{\rho}{2} [U_0^2 - |\nabla\psi|^2] \quad (41)$$

The force and moment of the contour can be computed by integration of the pressure around the contour.

#### INTERACTION EFFECT BETWEEN BODY AND CONTROL SURFACES

As indicated in Reference 9, the lift developed on a blunt-based body with fins as stern appendages can be calculated by using slender body theory to estimate the contributions of the body alone, the lift on the fins in presence of the body, and the lift on the body due to the fins. Alternatively, the lift on the fins alone can be estimated, as well as the ratio of the lift on the fin-body combination to that of the fins alone. In order to estimate the lift on the fins alone, the half-fins are joined together.

The method for estimating the lift developed on a submarine-like body with fins at the stern is discussed in Reference 13. In this reference, the lift on the fins alone is estimated by using the method provided in Reference 16. The contribution of the lift on the fins in presence of the body can be estimated by multiplying the lift developed on the fins alone by the empirical factor  $1 - r/(2b)$ , where  $r$  is the maximum radius of the body and  $b$  is the distance between the tip chord of the fin and the centerline of the body (outreach) for values of  $b/r$  between approximately 0.8 and 1.2. Since value of the ratio  $b/r$  is approximately 1.0 for the analysis performed herein, the empirical factor  $1 - r/(2b)$  would be approximately 0.5, and this value is used for the calculations herein.

## DISCUSSION OF NUMERICAL RESULTS

The results of calculations that have been made using the analytical method that has been developed are discussed herein. The empirical method for selecting the two-dimensional separation angles in the crossflow direction, the geometric characteristics of the configurations for which the calculations of the hydrodynamic forces and moments were performed, and the results of the calculations for the unappended hull, the control surfaces, and the partially appended body are discussed herein.

### TWO-DIMENSIONAL SEPARATION ANGLES IN CROSSFLOW DIRECTION

One of the most difficult tasks in this investigation was to determine the location of the separation line on the surface of the body. The hydrodynamic forces and moments developed on the body can not be predicted without knowing the location of the separation line accurately. Even though the velocity distribution on the surface of the body is computed accurately by solving the Navier-Stokes equations, there is poor agreement between the computations and the measured values of the hydrodynamic forces and moments. The reason for the poor agreement in the force and moment results is probably the inability to predict the exact location of the separation line in the computation process.

While the velocity distribution on the surface of the body is computed using potential flow theory, the location of the separation line must be accordingly compatible to the velocity distribution. The location of the separation line is a function of the Reynolds number, angle of attack or angle of drift, geometry of the body, and the turning rate. Figure 8 from Reference 10 shows the results of measurements of where the flow separates in the crossflow plane of a spheroid at angle of attack of 30 degrees. The figure shows that the angle at which separation occurs at the bow is larger than the angle at the stern.

In the analysis discussed herein, there was no attempt to determine the location of the separation line analytically. Instead, the hydrodynamic forces and moments were computed using an arbitrary location for the separation line, and the results of this calculation were compared with experimental data. Based on the comparison, the location for the separation line was changed and another calculation was made. After one or more additional calculations, the computed results for forces and moments and the experimental results agreed, and the location of the separation was determined. It was assumed that the location of the separation line was independent of the Reynolds number, the angle of attack, the geometry of the body, and the turning rate.

The fineness ratios of the nine configurations used for determining the location of the separation for straightline motion were between 4.0 and 12.4. The fineness ratios of the six configurations used for determining the location of the separation for the rotational motions were between 4.0 and 11.0. The values for the separation angles that were selected for straightline motion were 170 degrees at the bow and 110 degrees at the stern. The values selected for rotational motion were 160 degrees at the bow and 110 degrees at the stern. These separation angles were used for all of the calculations discussed herein.

## GEOMETRIC CHARACTERISTICS OF THE CONFIGURATIONS

To validate the present method the forces and moments of four configurations were computed and their results were compared with test results. Their geometric characteristics are given in Table 1. For a spheroid and the Akron, the forces and moments of the bare hull are computed. For Model 4621 and the DARPA SUBOFF, the results of bare hull and partially appended body are presented. The total number of discretized panels for the body surface is 280 for all of the models. Forces and moments are non-dimensionalized using  $\rho U_0^2 L^2/2$  and  $\rho U_0^2 L^3/2$ , respectively.

## RESULTS OF THE CALCULATIONS FOR THE UNAPPENDED HULL

To validate the present method to compute the axial force (Equation (10)), the computed axial forces of three different bodies of revolution are compared with test results for Reynolds numbers between 2 and 26 million. The results are shown in Figure 8. The agreement between the present method and test (Reference 11) is very good. The computed potential forces should be zero. However, small values of forces are computed. These small forces are caused by the numerical inaccuracy. The body surface is replaced with 280 quadrilateral elements. If the number of panels is increased, the potential forces will become smaller.

The results for the bare hull for straightline motion are given in Figures 9 through 12. Except for the axial forces, the computed vertical forces and pitching moments of spheroid agree very well with test results (Reference 12) for the entire range of angles of attack. The trend of the measured axial forces is different from those for other configurations as will be seen later. It is possible that there might be some errors in the measurements. The potential axial and vertical forces become zero as expected. For this model the numerical inaccuracy caused by discretization of the forebody cancels out that of after body.

The computed results of vertical forces and pitch moments of the Akron airship agree very well with test results (Reference 5). The computed axial forces show small discrepancies from test results. The discrepancies are caused by the fact that the potential axial forces are not completely zero. When the angle of attack is zero,  $C_x$  is computed -0.0002. If the number of panels is increased to 364,  $C_x$  is computed as -0.0001. The error analysis is given later in this report.

The computed results for the forces and moments for Model 4621 and the DARPA SUBOFF agree very well with test results as shown in Figures 11 and 12. The test results of Model 4621 and DARPA SUBOFF are taken from References 13 and 14, respectively.

The results for the bare hull for the rotational motion are given in Figures 13 and 14. The computed results of lateral forces and yaw moments of the spheroid agree fairly well with test results. The measured axial forces are not available. For this model the optimal two-dimensional separation angles are actually found as 160 and 120 degrees when the drift angle is negative, and 160 and 100 degrees when the drift angle is positive.

The results for Model 4621 are given in Figure 15 for four different turning rates. All computed forces and moments agree very well with unpublished test results. However, for small turning rates for which the model is far away

from the center of rotation, the computed axial forces at a drift angle of 20 degrees are larger than the test results, while for turning rates larger than 0.39 the computed axial forces agree very well with test results.

#### RESULTS OF THE CALCULATIONS FOR THE CONTROL SURFACES

To validate the present method of computing the forces and moment of a finite wing, which is described with Equations (28) through (32), the forces and moments of a finite wing with three different aspect ratios are computed and the results are given in Figure 15. The section shape of the wing is NACA 0015, its taper ratio is 0.45, and the sweep angle is zero. The details of the geometry and test results are given in Reference 15. Forces and moments are non-dimensionalized with  $\rho U^2 S_c/2$  and  $\rho U^2 b S_c/4$ , respectively.

The computed results for  $C_D$  drag and lift agree well with test results for all aspect ratios. The computed pitching moments with respect to the mean quarter-chord agree fairly well with test results when the angle of attack is less than 12 degrees and when the aspect ratios are 1 and 2. When the angle of attack is larger than 12 degrees, the computed pitching moments do not agree well with the test data. When the aspect ratio is 3, the computed pitching moments agree fairly well with test results for the entire range of angles of attack. An improvement in the theory is necessary for the computation of the pitching moment. It should be emphasized that a small error in predicting the center of pressure on a stern control surface does not have a significant effect on the estimate of the pitching moment which is resolved about the center of buoyancy.

#### RESULTS OF THE CALCULATIONS FOR THE PARTIALLY APPENDED BODY

The appendages used in the present validation are listed in Figure 17. Appendages 3A, 11A, 3B, 3C and the appendages for the SUBOFF are four identical cruciform planes. It is assumed that the geometrical angle of attack (Equation (28)) for the sternplanes or rudders for the straightline motion is the same as the angle of attack or drift angle of the body. The computed forces and moments of Model 4621 with Appendages 3A, 11A, and 3B agree very well with the test results for the entire range of angles of attack as shown in Figure 18. In the computed vertical forces and pitching moments, there is, of course, no contribution of the rudder to the total normal forces and moments. However, in the computed axial forces, there is a contribution from rudder.

The computed results for the SUBOFF model with bridge fairwater and stern appendage agree very well with test results for drift angles between -20 and 20 degrees as shown in Figures 19 and 20.

The computed results for Model 4621 with Appendage 3C are plotted in Figure 21 for three different turning rates. When an appended body is undergoing a rotational motion, the geometric angle of attack of the rudder in Equation (28) is not same as the drift angle. For Model 4621 it has been found that the geometric angles of attack are 3.4, 9.5, and 15.1 degrees larger than the angle

of drift at the center of rotation for turning rates 0.142, 0.399, and 0.639, respectively.

As shown in Figure 21, the computed results agree well with test results. Even though test results are shown for drift angles are between -5 and 10 degrees, the numerical results indicate good agreement over the full range of higher drift angles.

#### UNCERTAINTY ANALYSIS FOR THE NUMERICAL PROCEDURES

The major error in the numerical procedures for the present method occurs in the numerical evaluation of the kernel function of Equation (9). The surface area of the body is discretized, the source and sink strengths are assumed constant on each discretized element, and the double integral in Equation (9) is evaluated numerically on each element. For the present presentation of numerical results, the number of discretized elements is 280 for all of the configurations. The larger the number of elements is, the more accurate the numerical results are.

To estimate the errors in the numerical procedures, the computed results are compared with the exact solution. The d'Alembert paradox says that the forces around a body in potential flow become zero regardless of angle of attack (see Reference 16). Table 2 shows the potential flow results for the axial and normal forces of the Akron airship which are dependent on the number of elements. As shown in this table, the computed forces becomes smaller and smaller as the number of elements increases. When the angle of attack is zero, the normal forces for different numbers of elements are all zero. While the flow on the body surface is symmetric with respect to the horizontal plane through the axis of symmetry, the numerical errors for the upper section of the body cancel out the errors for the lower section of the body. The axial forces were calculated to be non-zero, and these forces become smaller as the number of elements increases.

When the angle of attack is 21 degrees, then the normal force is, of course, non-zero. In this case the flow on the body surface is not symmetric with respect to the horizontal plane and therefore, the normal forces are computed as non-zero values.

As can be seen in Table 2, as the number of elements increases, the values calculated for  $C_x$  and  $C_z$  become smaller and approaches zero. The ratio of the values of  $C_x$  and  $C_z$  to the values of  $C_x$  and  $C_z$  calculated for 280 elements is tabulated. As can be seen the ratio becomes smaller.

#### CONCLUSIONS

The analytical method to predict forces and moments for a body of revolution with and without appendages has been developed and the numerical results for several configurations show very good agreements with test results. The present method can be applied to predict the in-plane forces and moments of body of revolution with and without appendages. The present method can be easily extended to the computation of roll moment and the out-of-plane forces and moments.

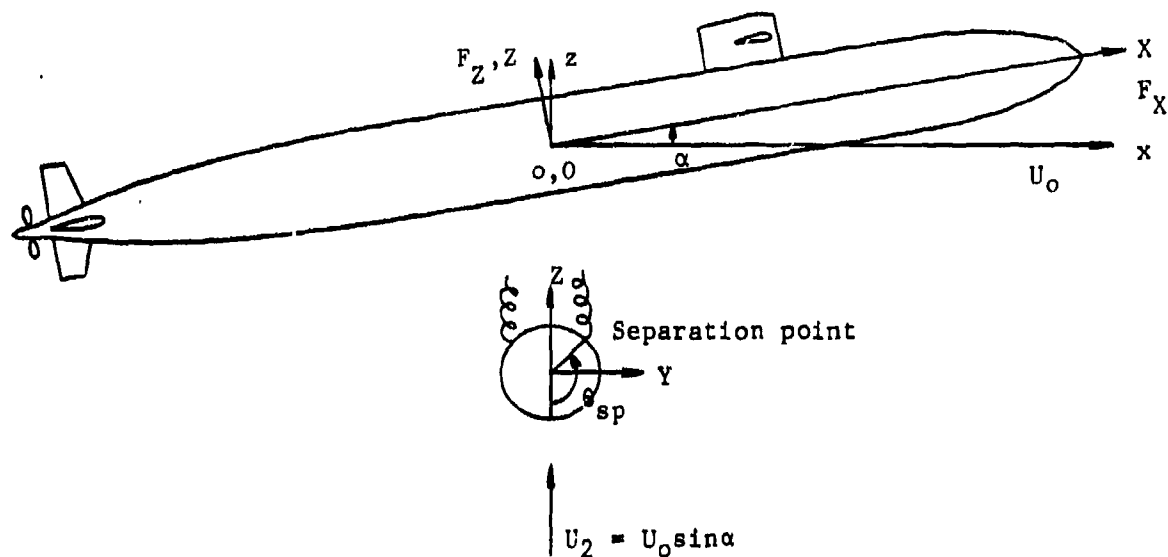
## RECOMMENDATIONS

It is recommended that the following work be undertaken to upgrade the method developed herein:

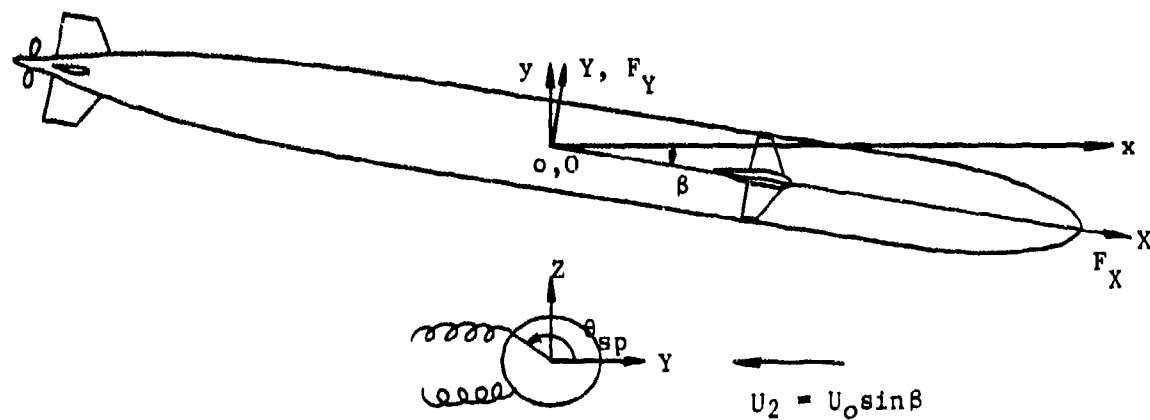
1. The method should be extended to include the prediction of the forces and moments for fully appended bodies, and the results should be applied to the analysis of the stability and control characteristics of submarines.
2. The method should be extended to include free-surface effects.
3. A more accurate method should be developed for determining the location of the lines of separation in order to improve the prediction of the forces and moments at large angles of attack.
4. The method should be extended to predict the forces and moments of a body of revolution undergoing combined pitching and yawing angular velocities.

## ACKNOWLEDGMENTS

Ms. Elizabeth Dempsey and Mr. Richard Curphey provided valuable information about the experimental data that is discussed in this report. Dr. Jerome Feldman provided technical guidance and reviewed the report.



(a) Vertical plane



(b) Horizontal plane

Fig. 1 - Coordinate system for the straight-line motion



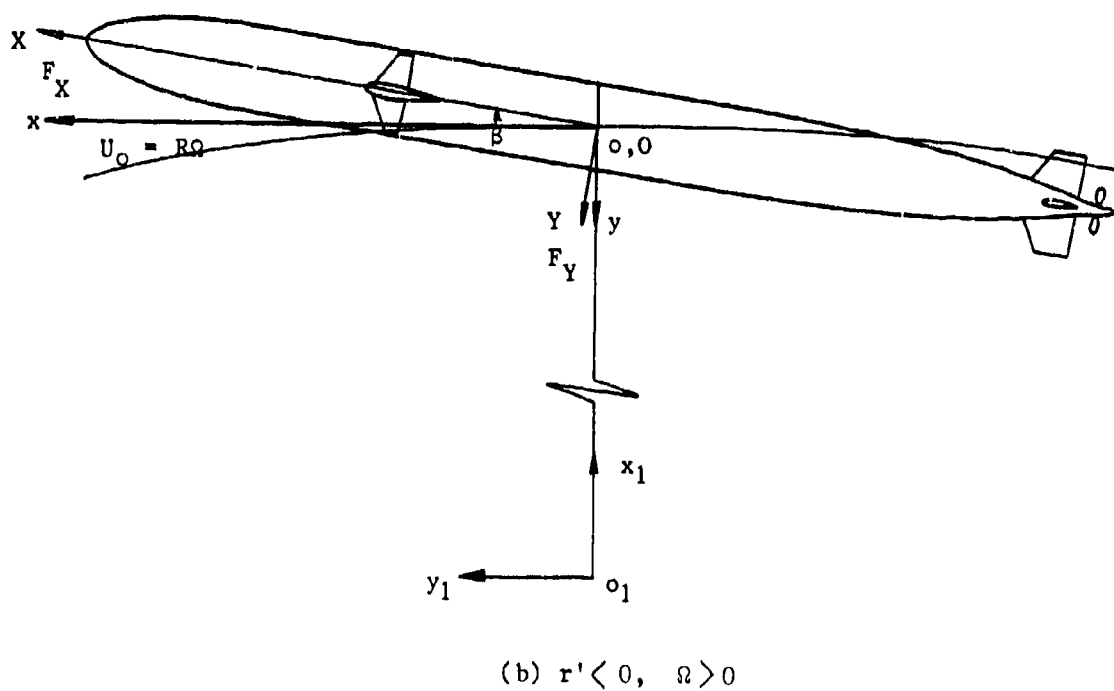
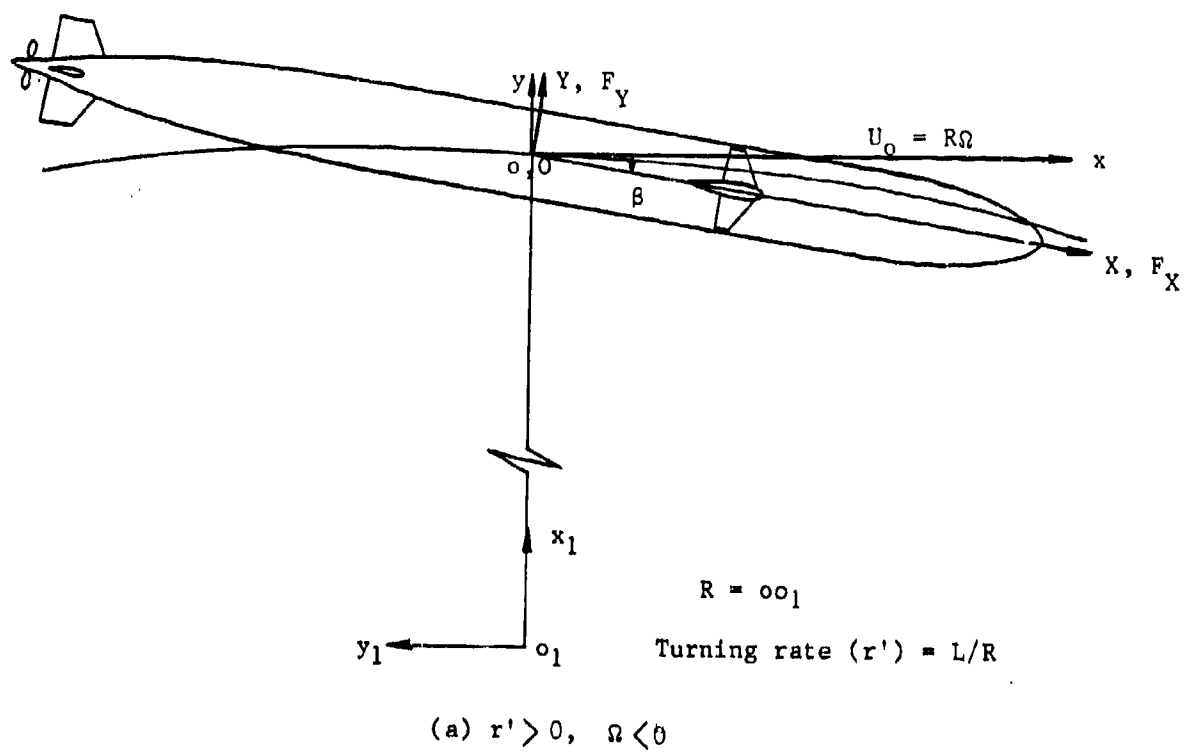


Fig. 2 - Coordinate system for the rotational motion

LEGEND  
 □ - POTENTIAL VELOCITY  
 ○ - EXTRAPOLATED VELOCITY  
 Δ - EXPERIMENTAL VELOCITY

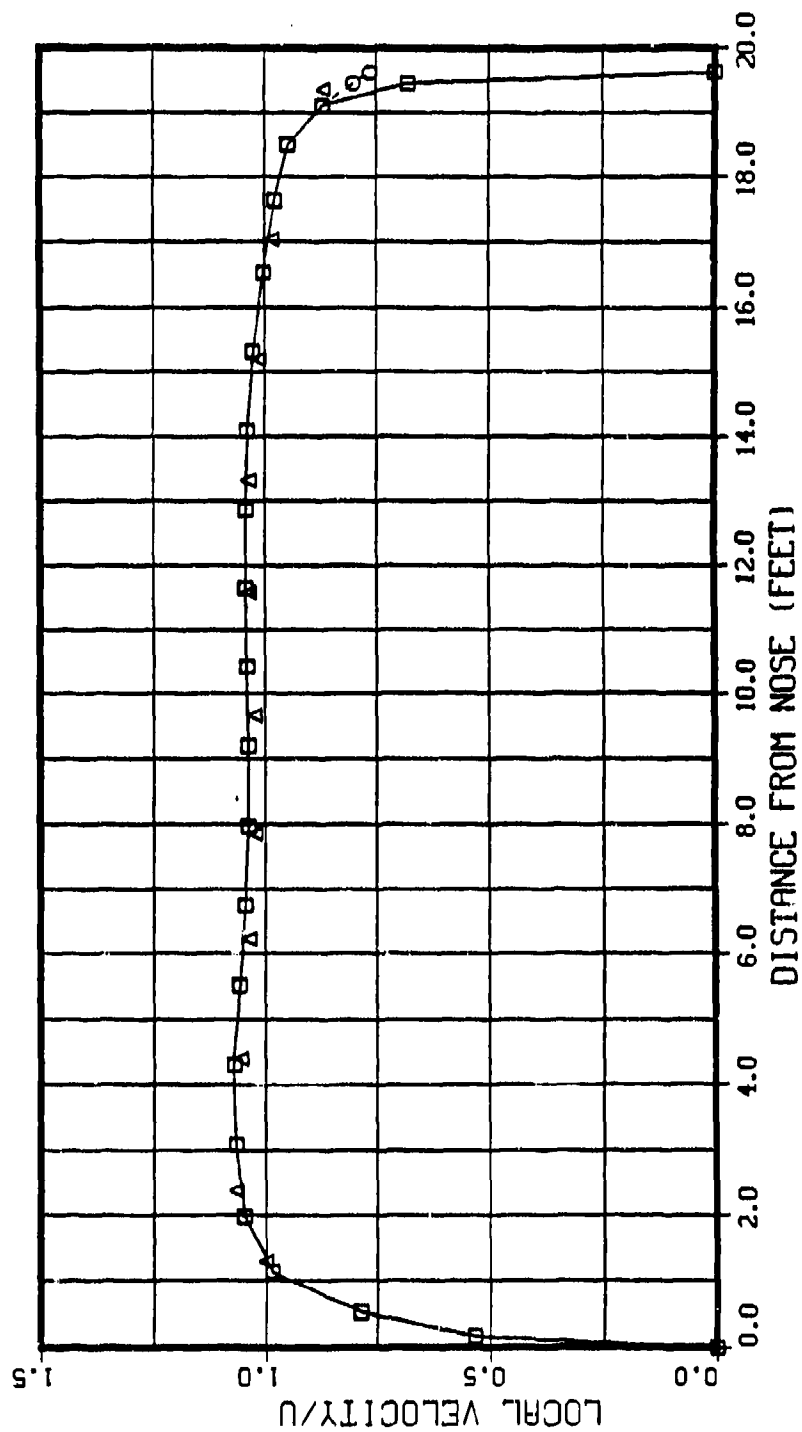


Fig. 2 - Axial velocity of the Akron airship when  $\alpha = 0$  degree

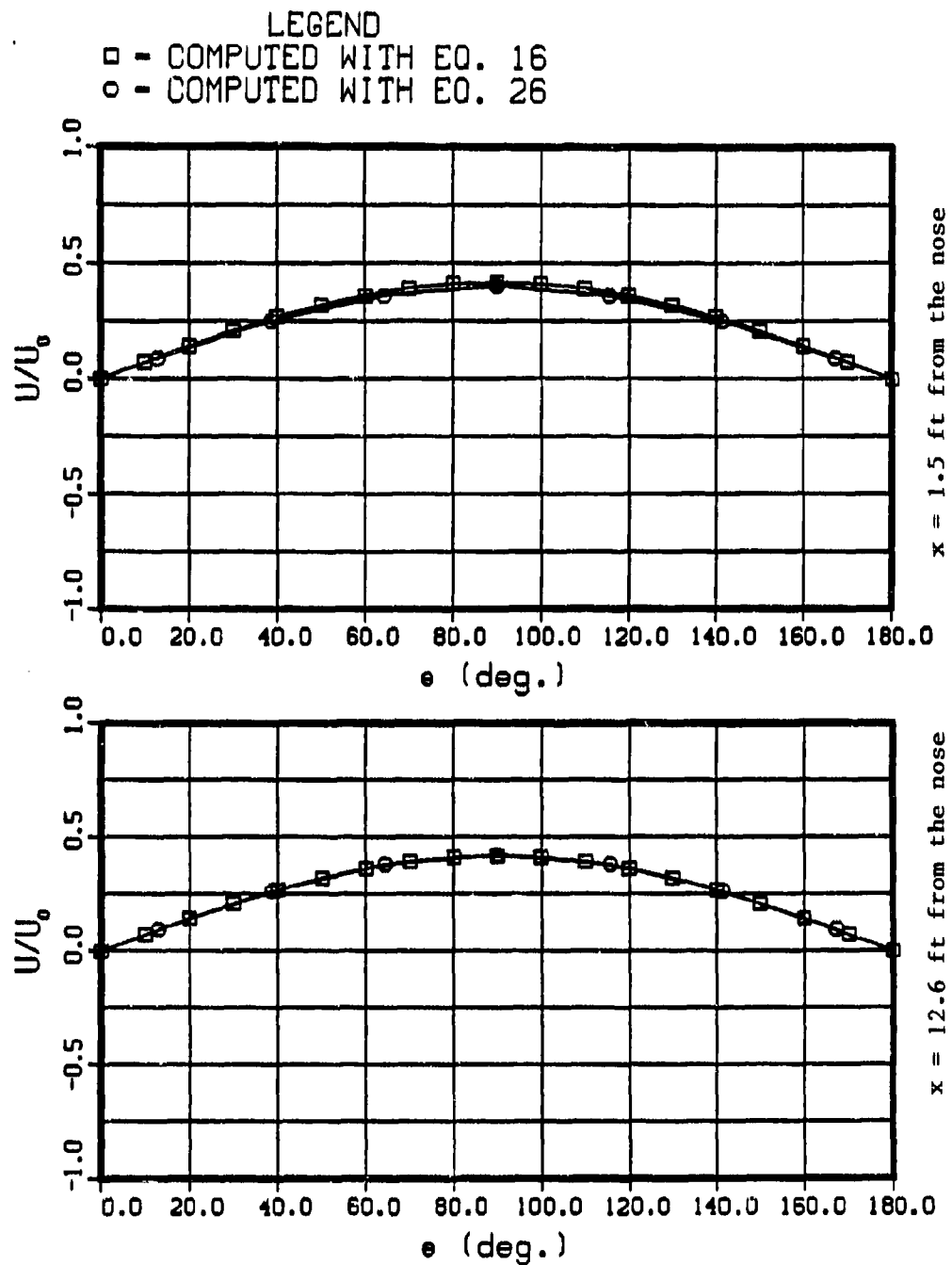


Fig. 4 - Tangential velocity of Model 4621 in the crossflow direction when  $\alpha = 12$  degrees

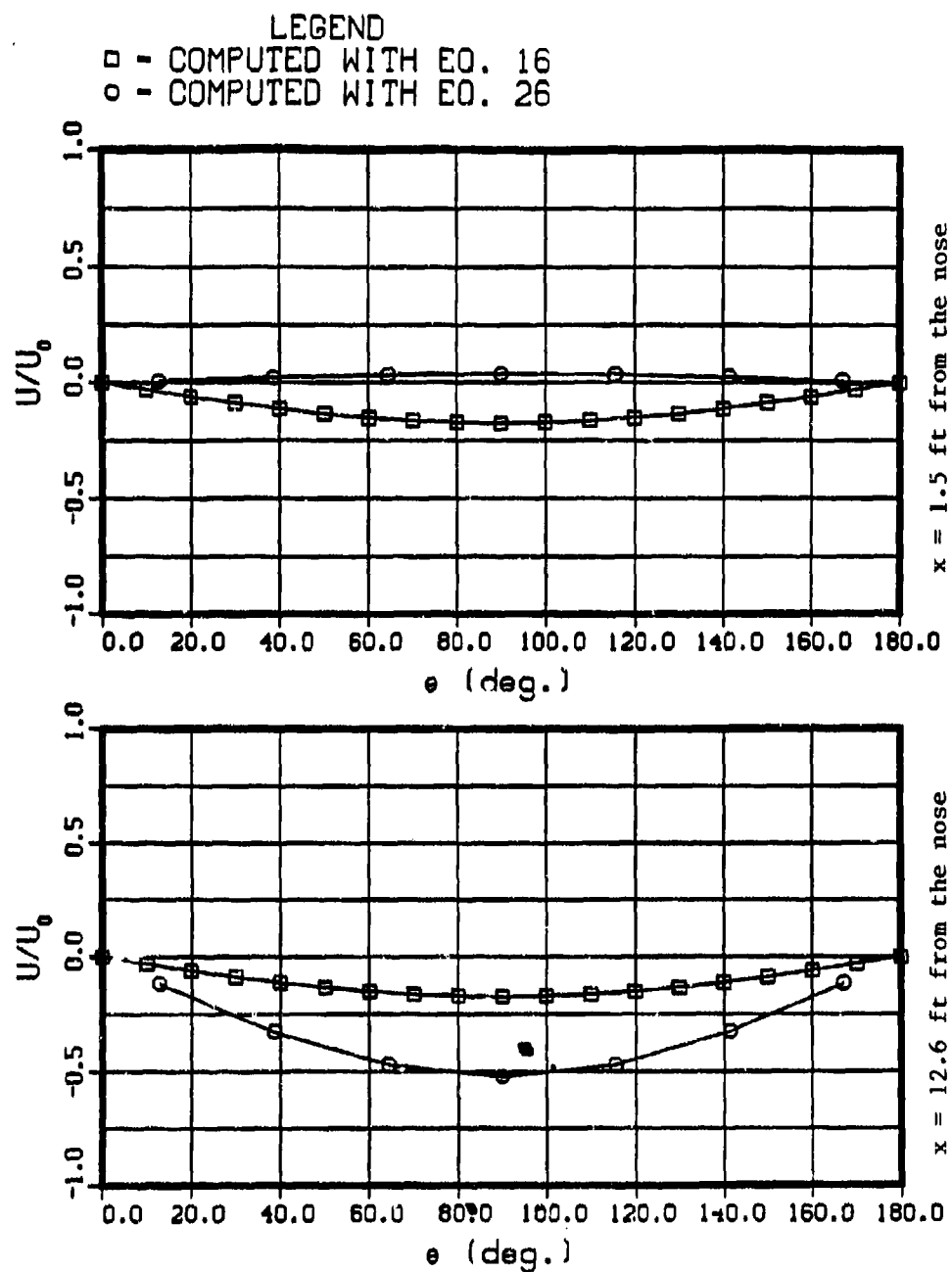
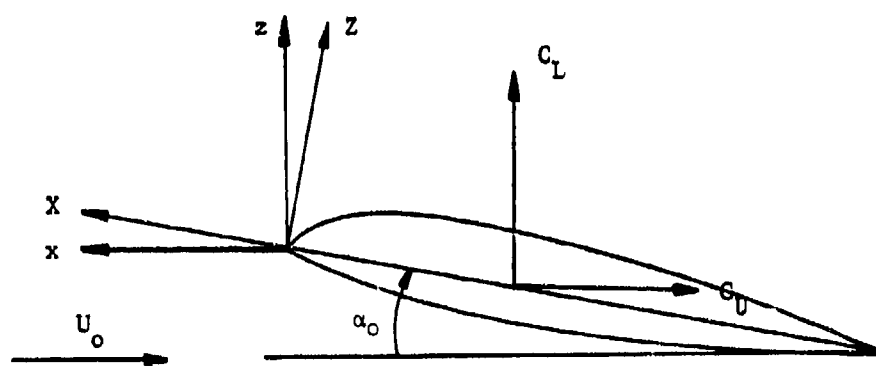
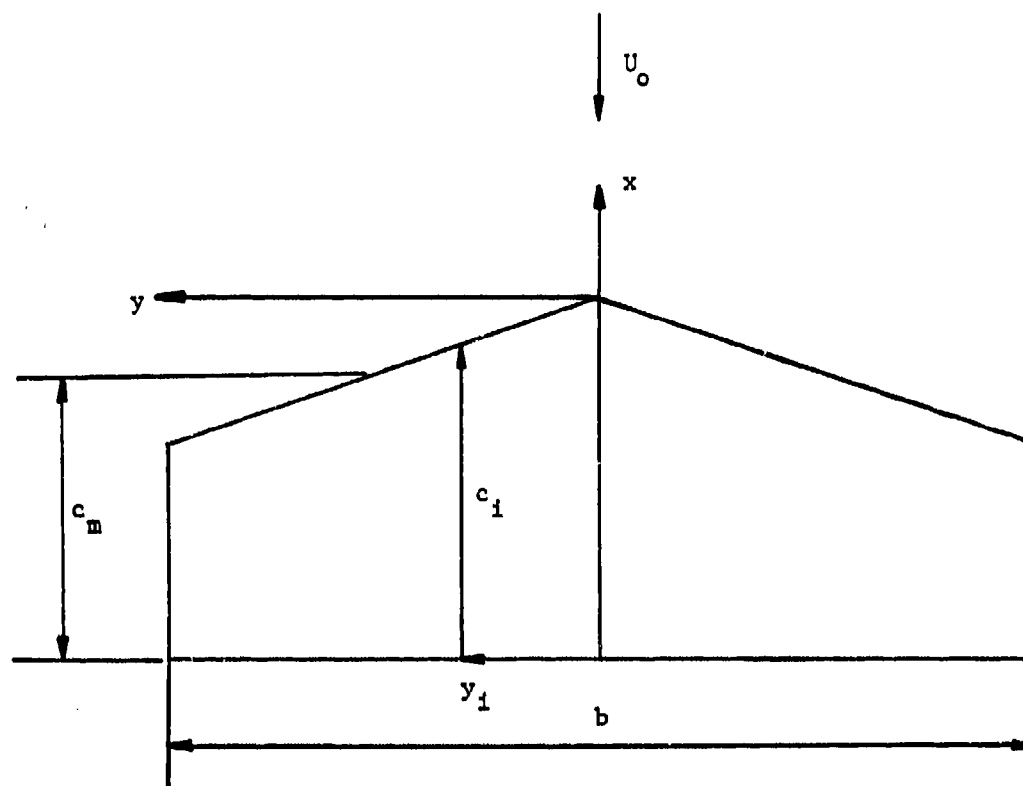


Fig. 5 - Tangential velocity of Model 4621 in the crossflow direction when  $\beta = 5$  degrees and  $n' = 0.389$



Aspect ratio (A) =  $b/c_m$

Fig. 6 - Coordinate system for a finite wing

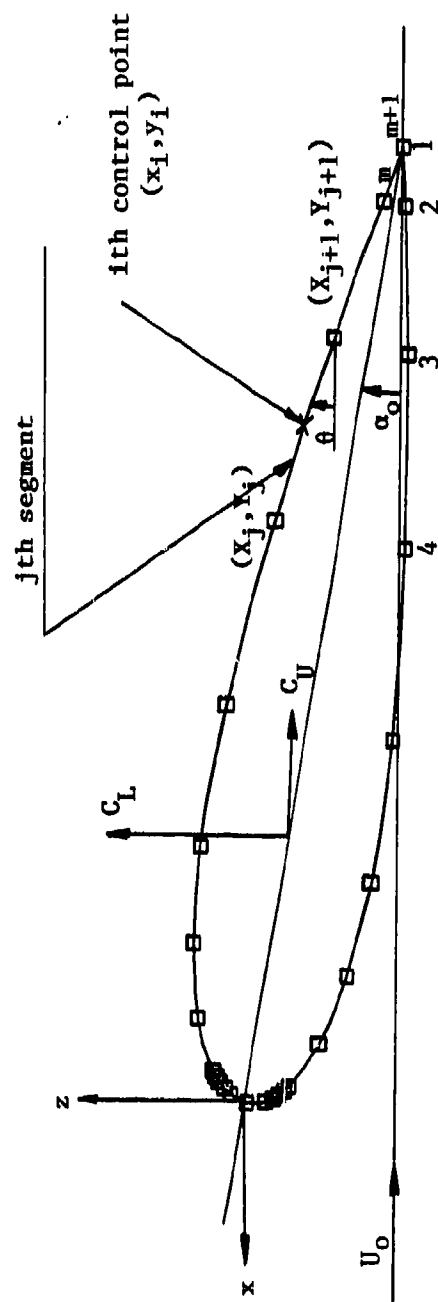


Fig. 7 - Sectional contour of a finite wing

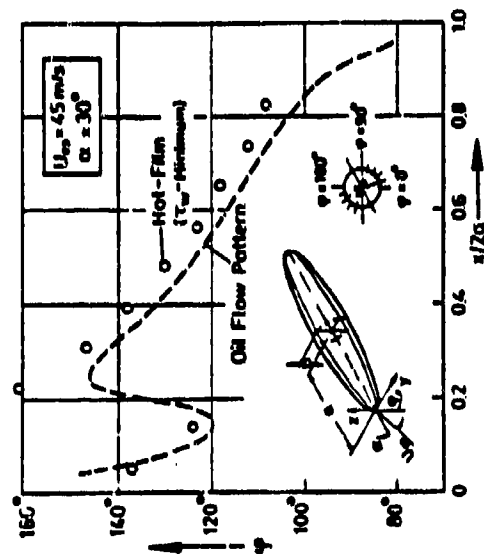


Fig. 8 - Measured separation angles of a spheroid when  $\alpha = 30$  degrees (Ref. 10)

LEGEND  
 □ - COMPUTED TOTAL FORCE  
 ○ - COMPUTED POTENTIAL FORCE  
 △ - EXPERIMENTAL TOTAL FORCE

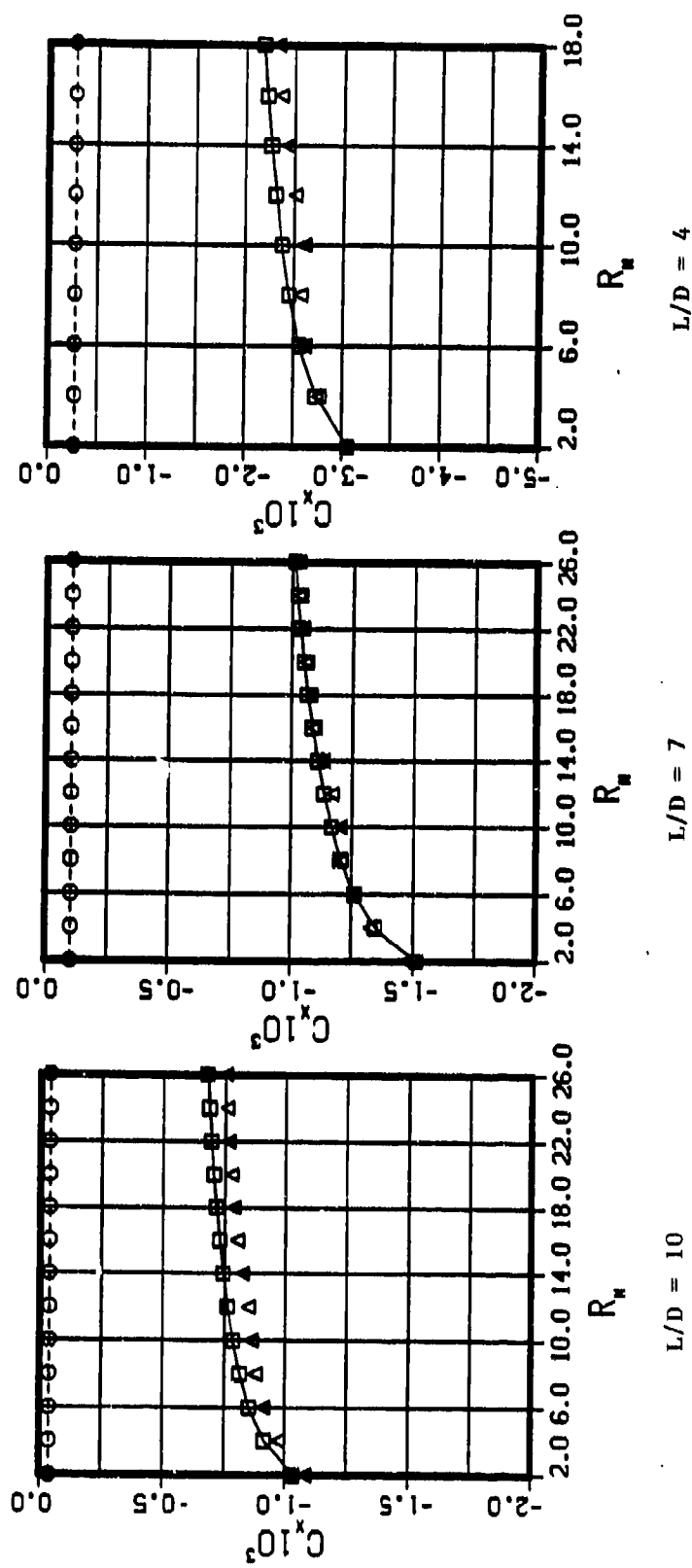


Fig. 9 - Axial forces of Series 58 when  $\alpha = 0$  degree



LEGEND  
 □ - COMPUTED TOTAL FORCE  
 ○ - COMPUTED POTENTIAL FORCE  
 Δ - EXPERIMENTAL TOTAL FORCE

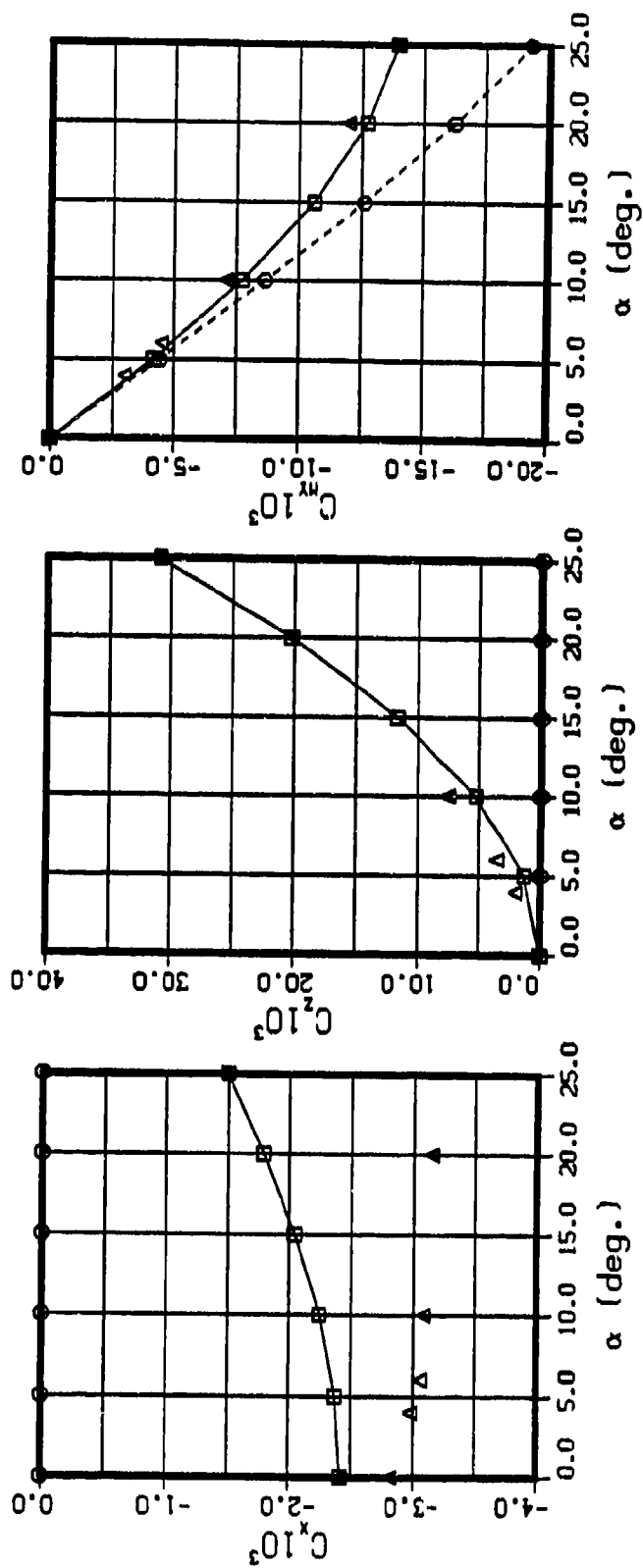


Fig. 10 - Forces and moments of a spheroid with  $L/D=4$  for straightline motion

LEGEND  
 □ - COMPUTED TOTAL FORCE  
 ○ - COMPUTED POTENTIAL FORCE  
 Δ - EXPERIMENTAL TOTAL FORCE

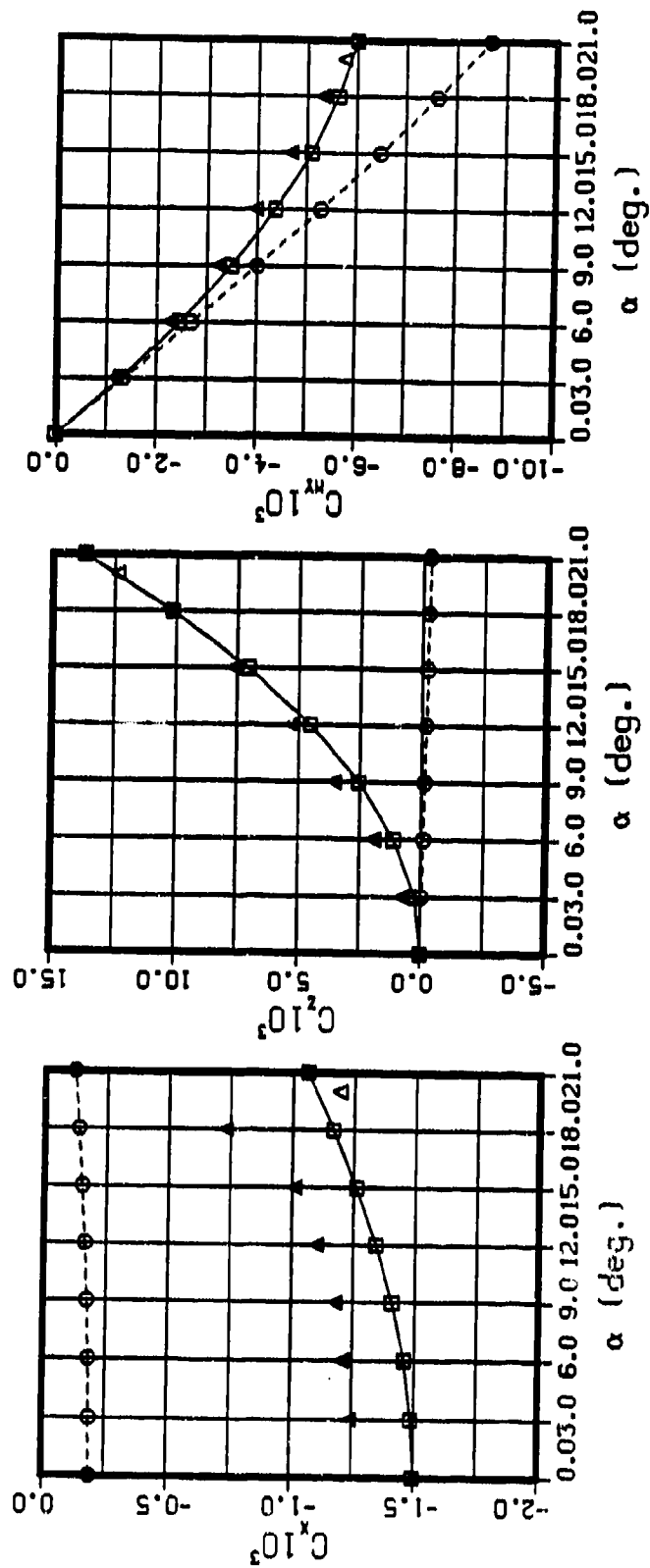


Fig. 11 - Forces and moments of the Akron airship for straightline motion

LEGEND  
 □ - COMPUTED TOTAL FORCE  
 ○ - COMPUTED POTENTIAL FORCE  
 Δ - EXPERIMENTAL TOTAL FORCE

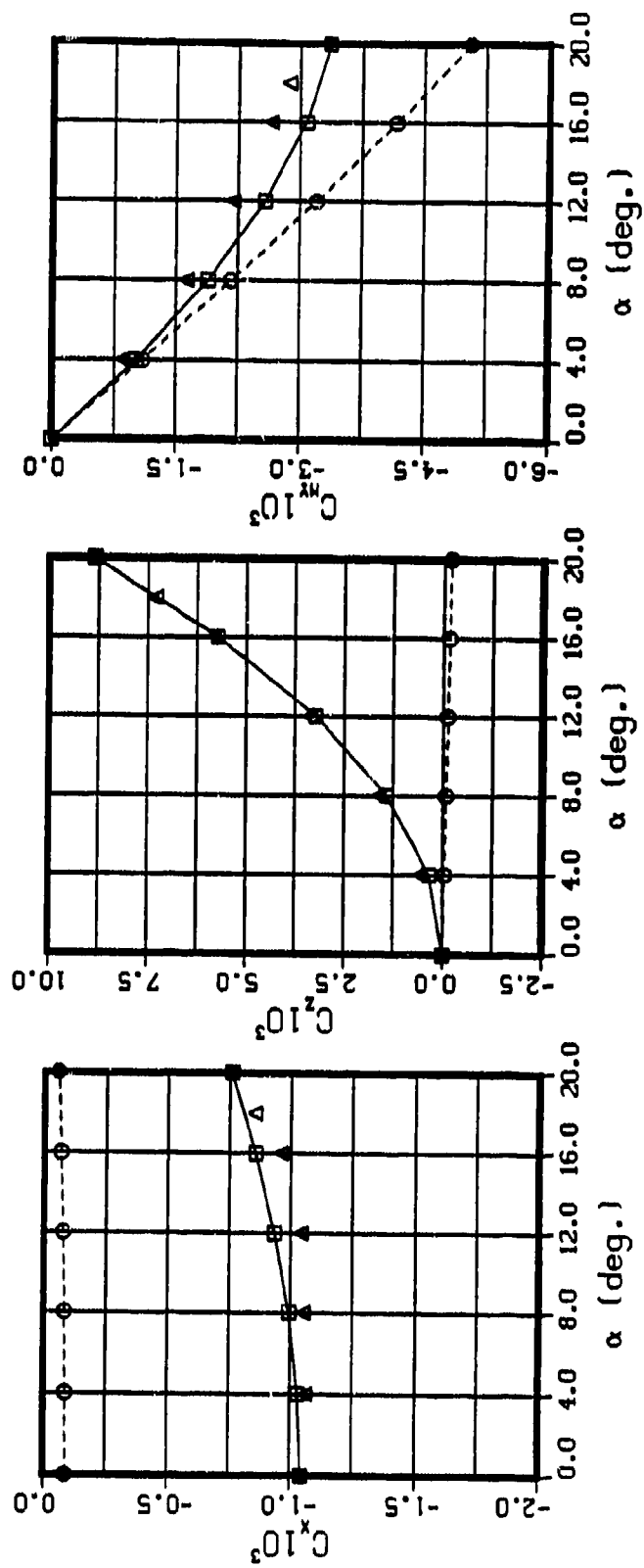


Fig. 12 - Force components and moments of Model 4621 for straightline motion

LEGEND  
 □ - COMPUTED TOTAL FORCE  
 ○ - COMPUTED POTENTIAL FORCE  
 △ - EXPERIMENTAL TOTAL FORCE

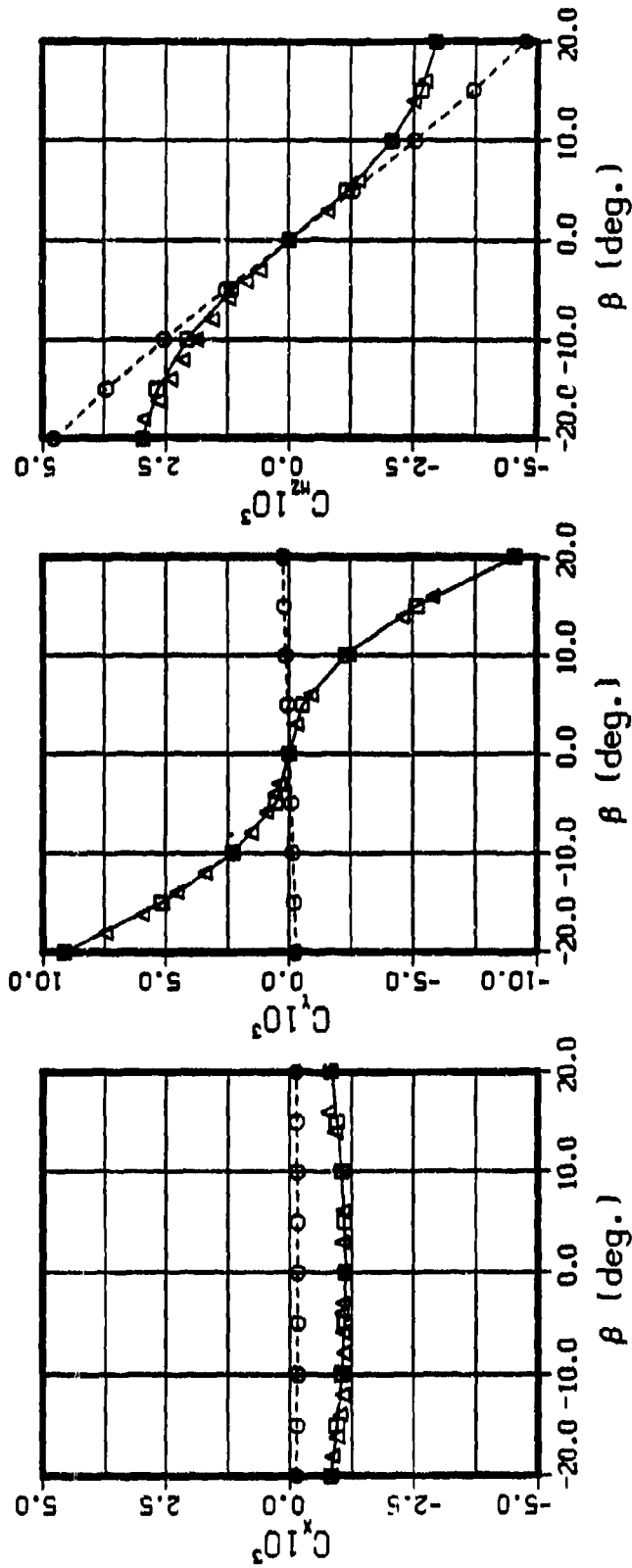


Fig. 13 - Forces and moments of the DARPA SUBOFF for straightline motion

LEGEND  
 □ - COMPUTED TOTAL FORCE  
 ○ - COMPUTED POTENTIAL FORCE  
 Δ - EXPERIMENTAL TOTAL FORCE

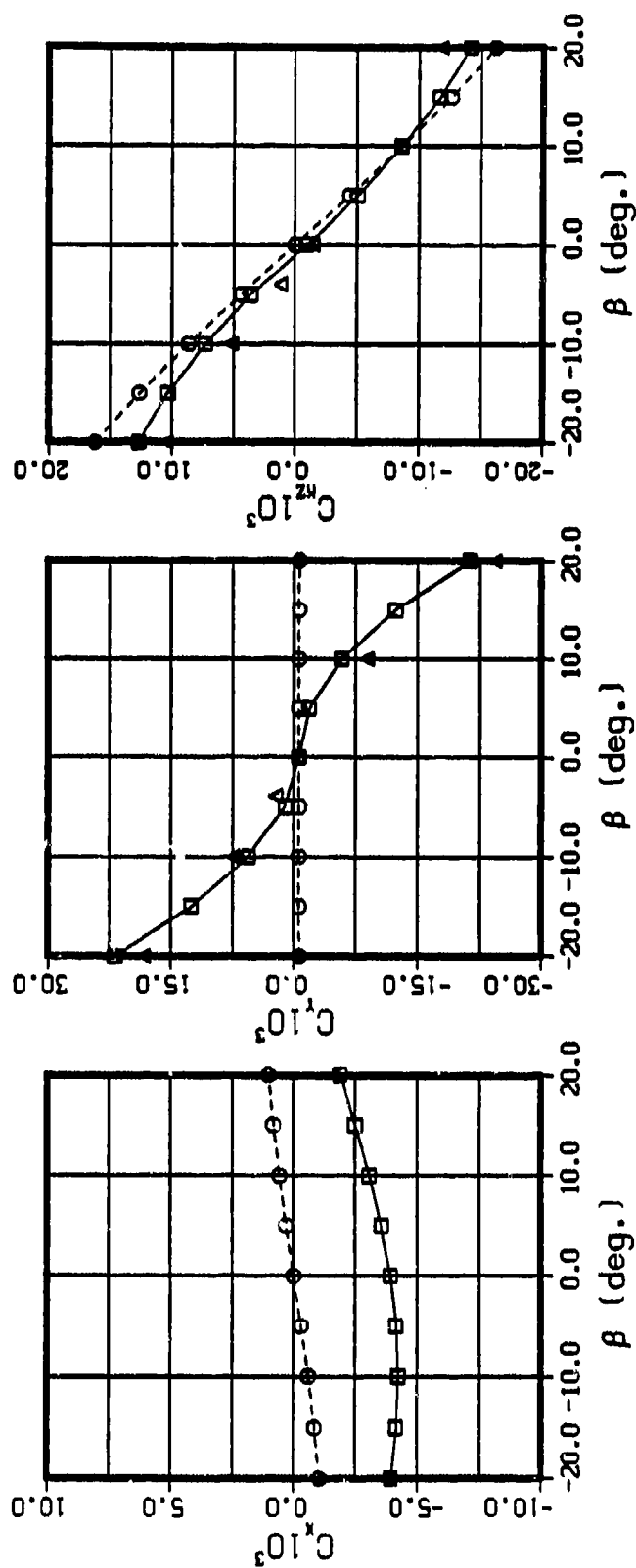


Fig. 14 - Force components of a spheroid with  $L/D=4$  for rotational motion with  $r' = -0.072$

LEGEND  
 □ - COMPUTED TOTAL FORCE  
 ○ - COMPUTED POTENTIAL FORCE  
 △ - EXPERIMENTAL TOTAL FORCE

(a)  $r' = 0.137$

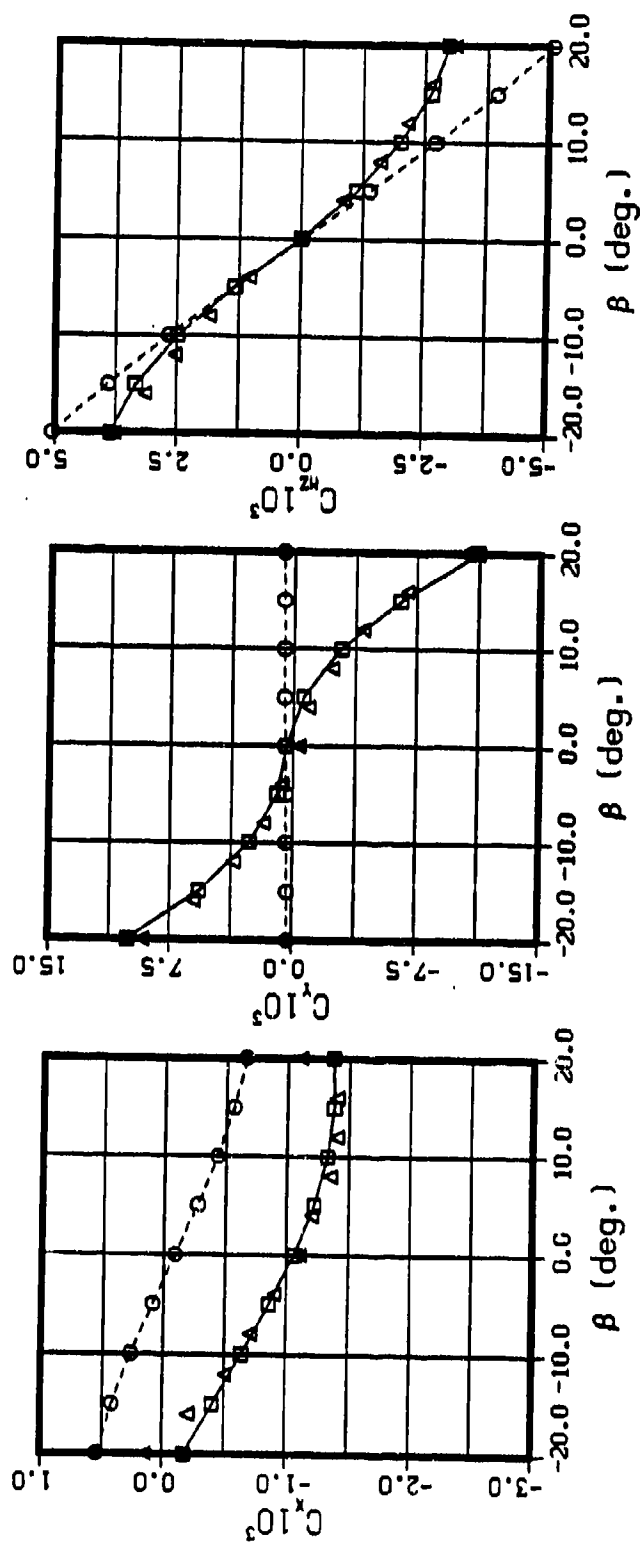


Fig. 17 - Forces and moments of Model 4621 for rotational motion

LEGEND  
 □ - COMPUTED TOTAL FORCE  
 ○ - COMPUTED POTENTIAL FORCE  
 Δ - EXPERIMENTAL TOTAL FORCE

(b)  $r^* = 0.399$

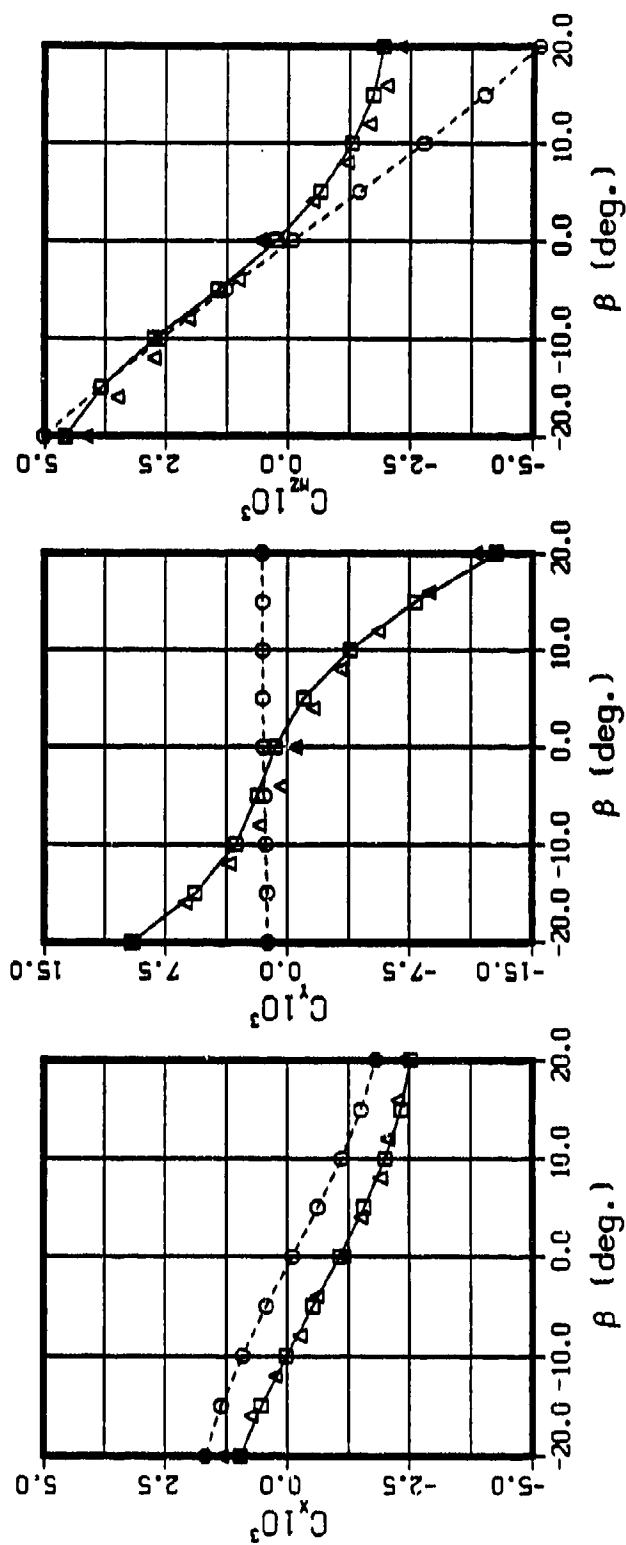


Fig. 15 - Continued

LEGEND  
 □ - COMPUTED TOTAL FORCE  
 ○ - COMPUTED POTENTIAL FORCE  
 Δ - EXPERIMENTAL TOTAL FORCE

(c)  $r' = 0.639$

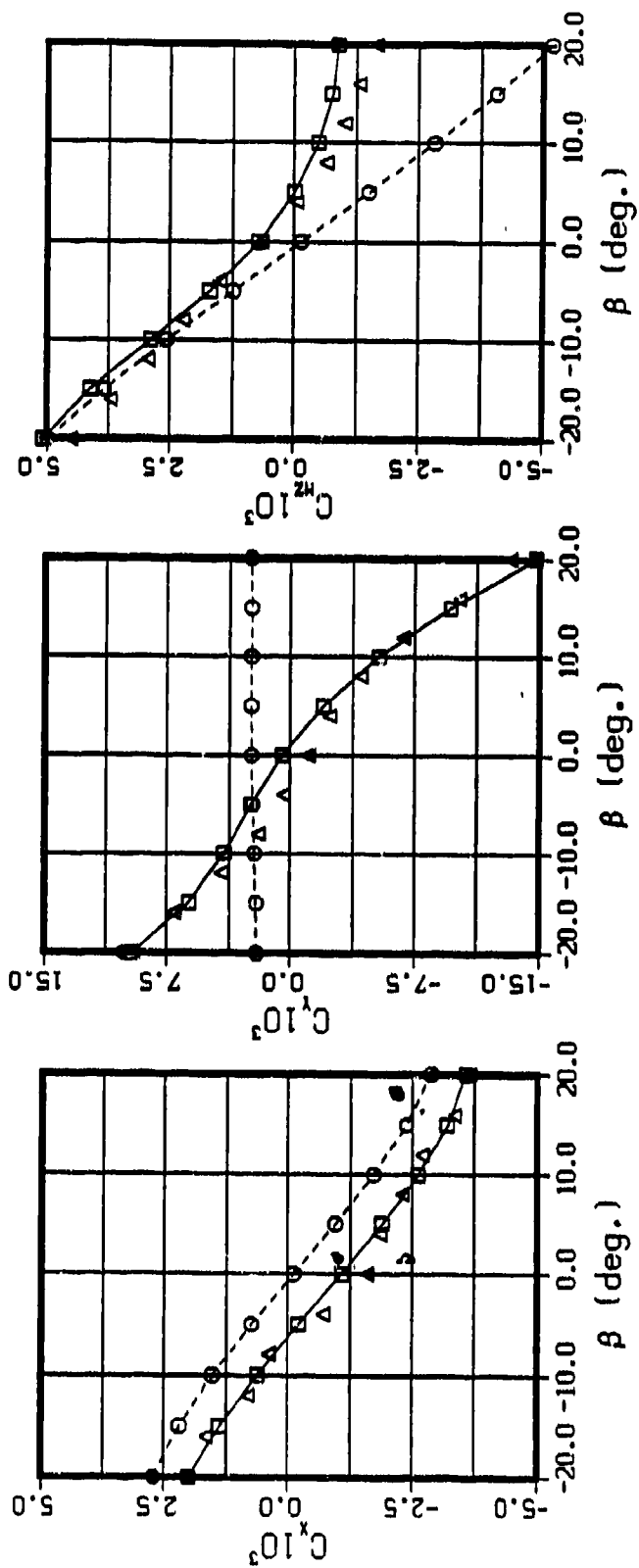


Fig. 15 - Continued



LEGEND  
 □ - COMPUTED TOTAL FORCE  
 ○ - COMPUTED POTENTIAL FORCE  
 Δ - EXPERIMENTAL TOTAL FORCE

(a)  $\Lambda = 1$

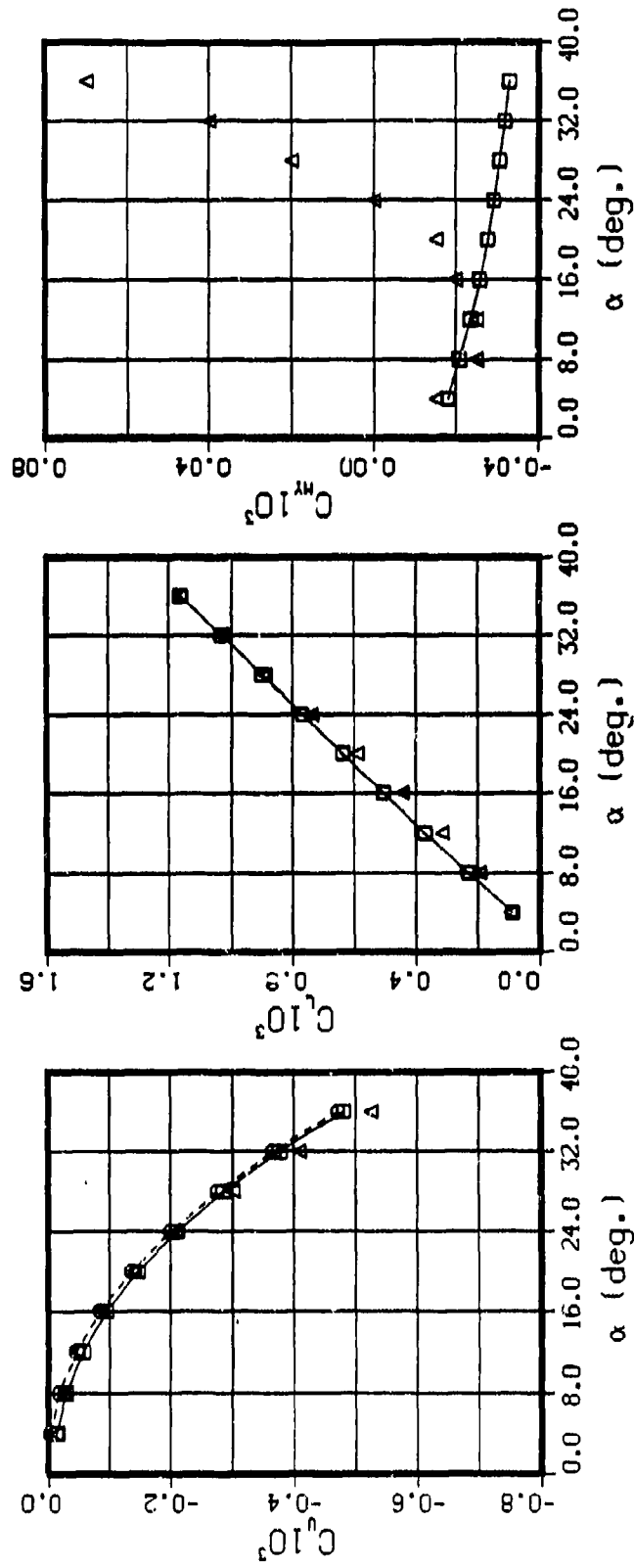


Fig. 10.  $C_u$ ,  $C_l$ , and  $C_m$  vs  $\alpha$  for a finite wing with an NACA 0015 section shape.

LEGEND  
 □ - COMPUTED TOTAL FORCE  
 ○ - COMPUTED POTENTIAL FORCE  
 △ - EXPERIMENTAL TOTAL FORCE

(b)  $A = 2$

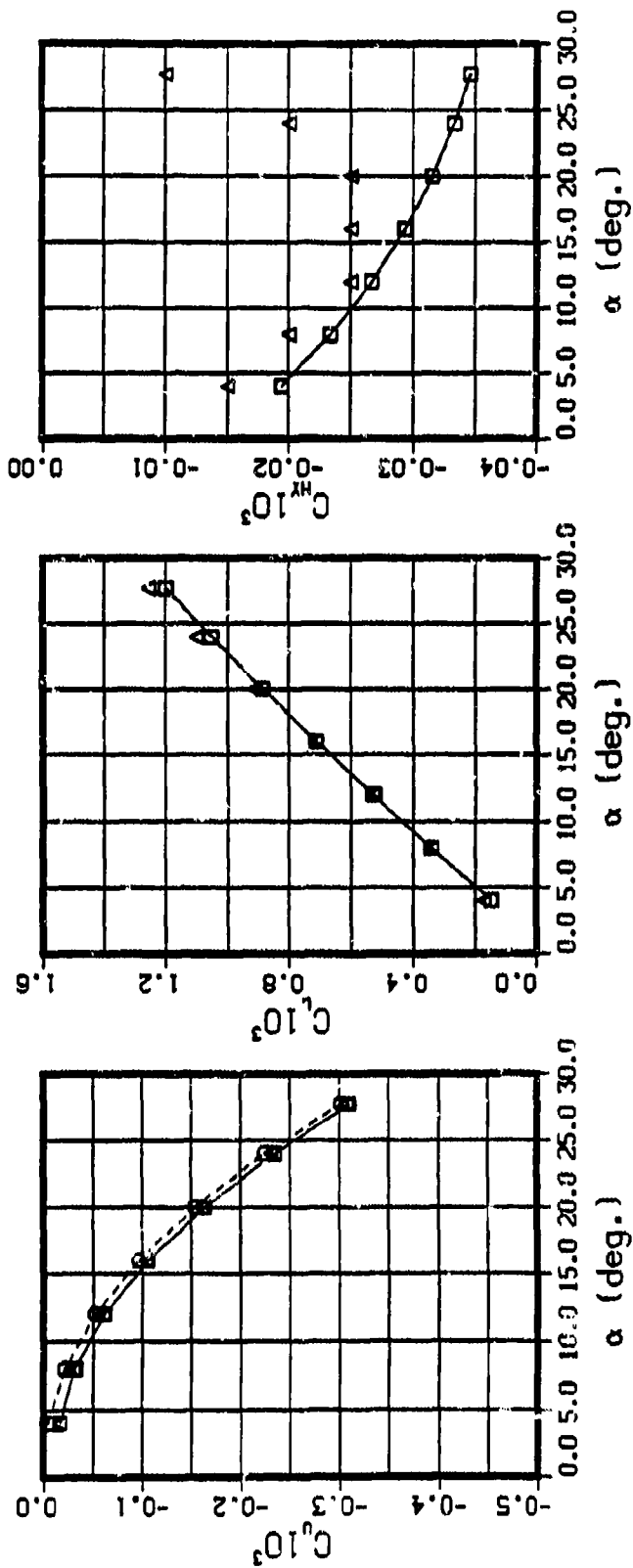


Fig. 16 - Continued

LEGEND  
 □ - COMPUTED TOTAL FORCE  
 ○ - COMPUTED POTENTIAL FORCE  
 △ - EXPERIMENTAL TOTAL FORCE

(c)  $A = 3$

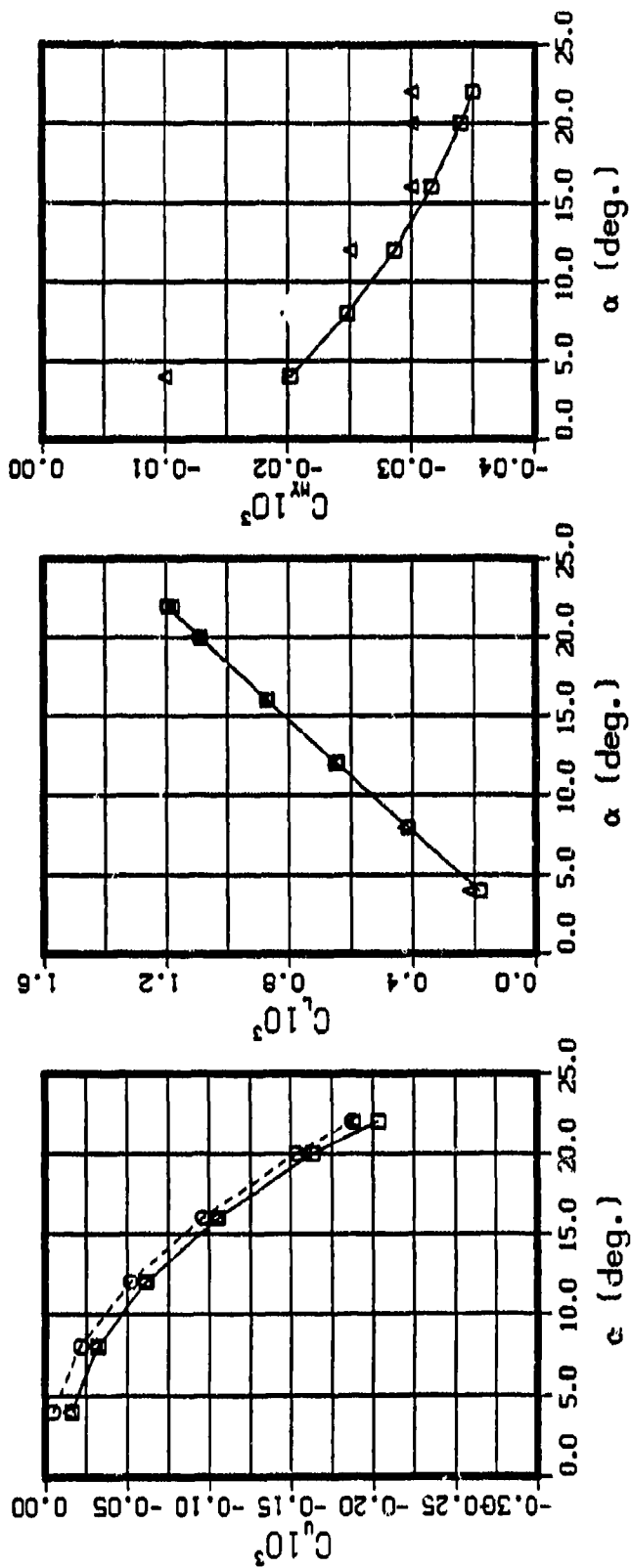
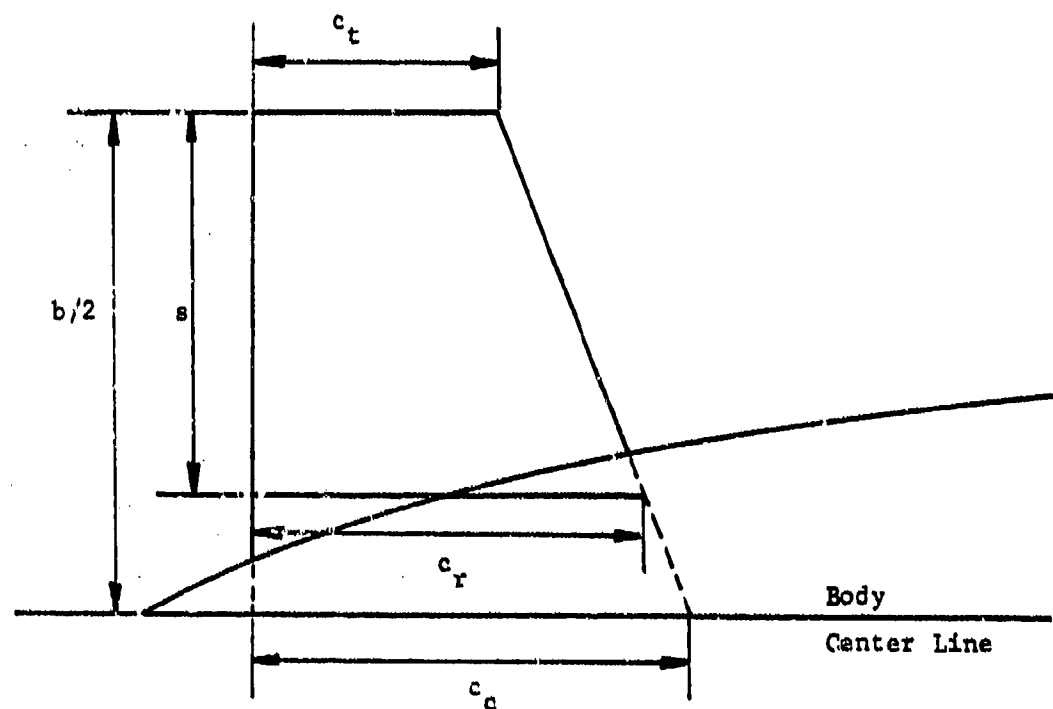


Fig. 16 - Continued



	3A	11A	3B	3C
$c_t$	0.250	0.917	0.250	0.250
$c_r$	0.437	1.080	0.525	0.598
$c_m$	0.344	0.999	0.388	0.424
$s$	0.513	0.448	0.755	0.955
$c_c$	0.523	1.190	0.614	0.690
$b/2$	0.750	0.750	1.000	1.208
$A_e = 2s/c_m$	2.987	0.897	3.897	4.505
$A_c = b/c_m$	3.881	1.424	4.630	5.140

Fig. 17 - Geometric characteristics of the appendages

LEGEND  
 □ - COMPUTED TOTAL FORCE  
 ○ - COMPUTED POTENTIAL FORCE  
 △ - EXPERIMENTAL TOTAL FORCE

(a) with appendage 3A

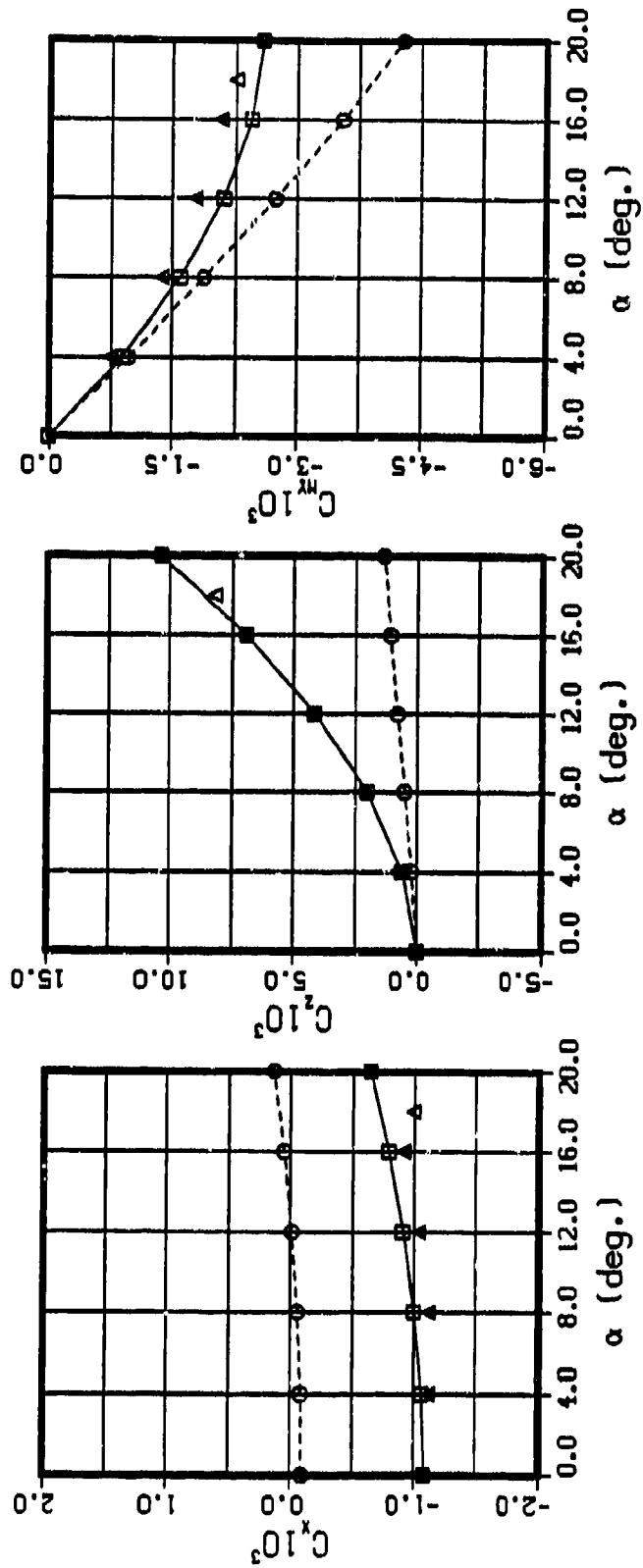


Fig. 10 Forces and moments of Model 4621 with appendage for straightline motion

LEGEND  
 □ - COMPUTED TOTAL FORCE  
 ○ - COMPUTED POTENTIAL FORCE  
 Δ - EXPERIMENTAL TOTAL FORCE

(b) with appendage 3B

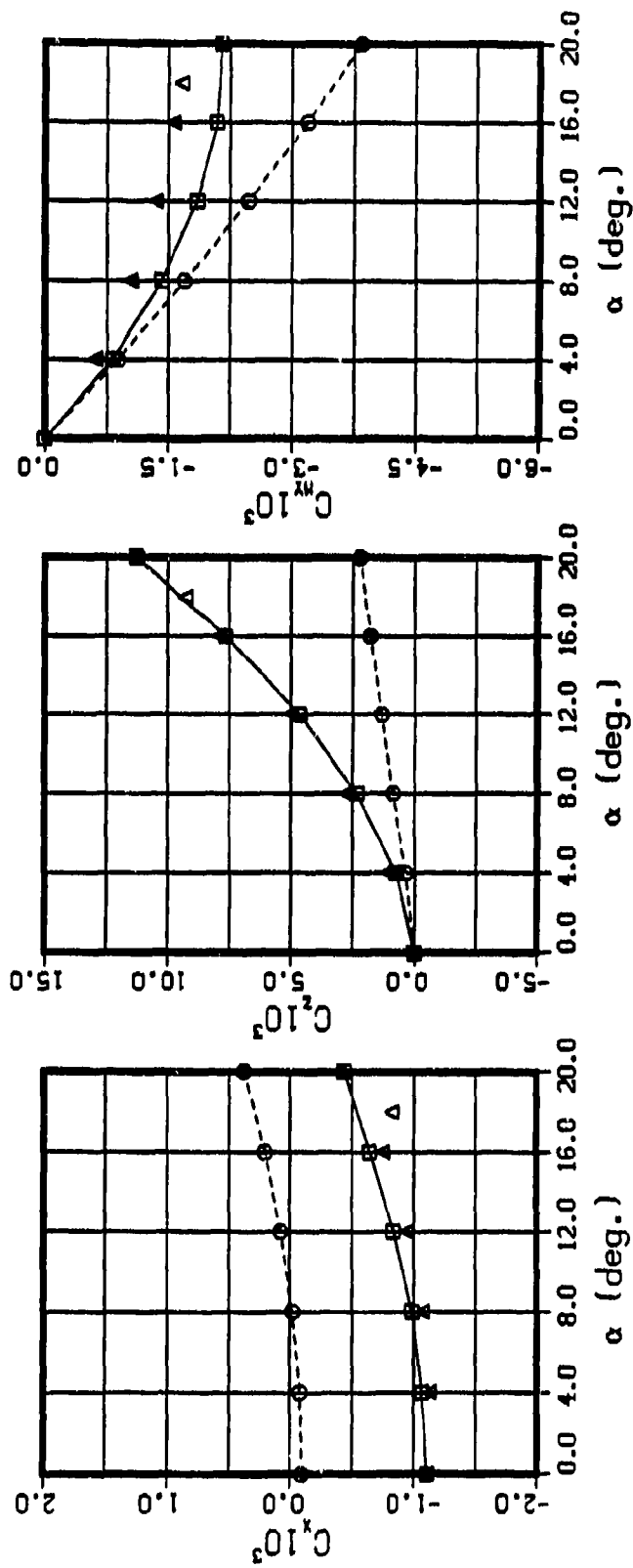


Fig. 18 - Continued

LEGEND  
 □ - COMPUTED TOTAL FORCE  
 ○ - COMPUTED POTENTIAL FORCE  
 Δ - EXPERIMENTAL TOTAL FORCE

(c) with appendage 11A

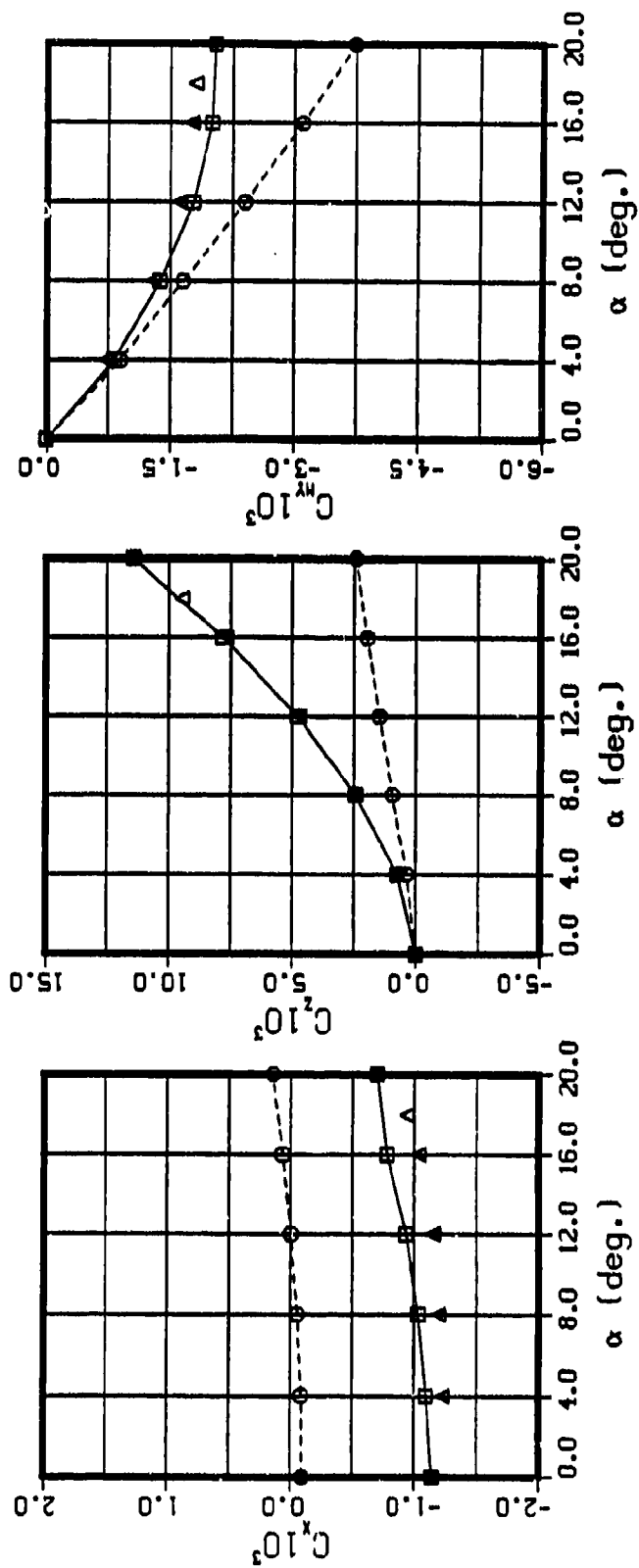


Fig. 18 - Continued

□ - COMPUTED TOTAL FORCE  
 ○ - COMPUTED POTENTIAL FORCE  
 △ - EXPERIMENTAL TOTAL FORCE

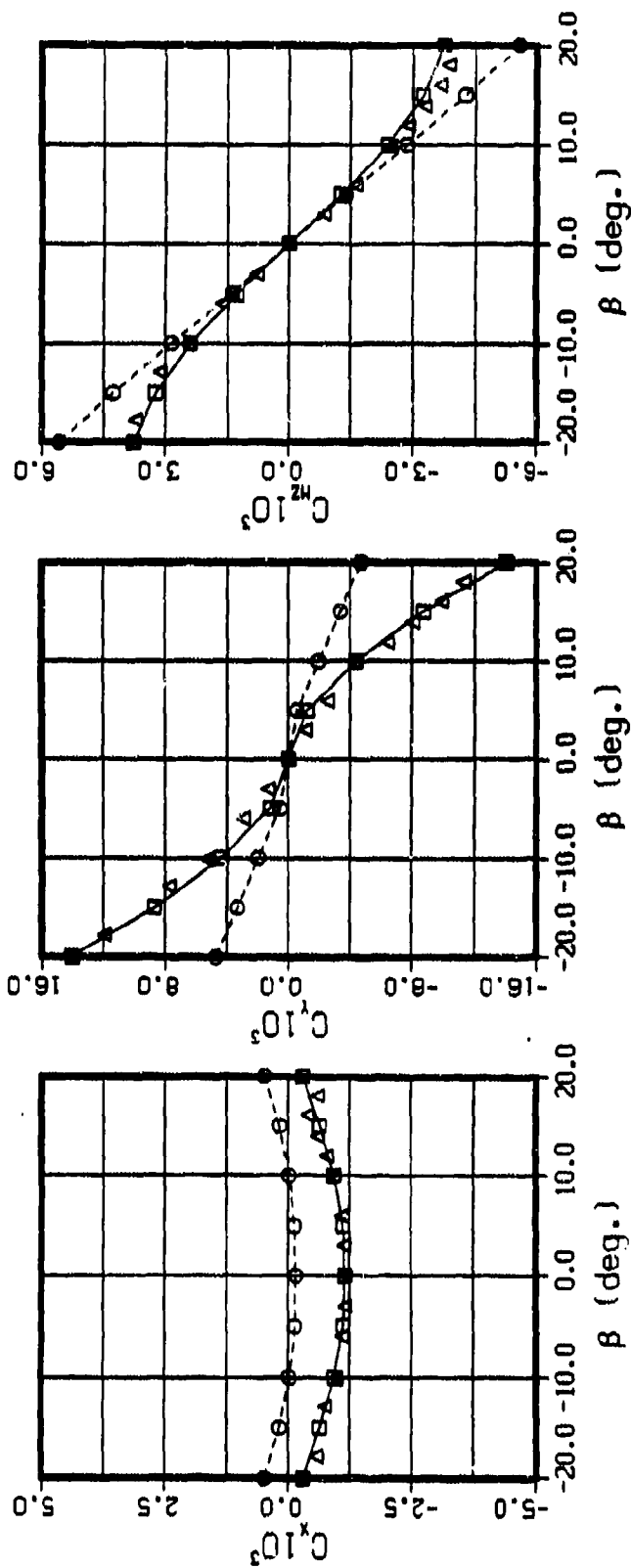


Fig. 10. Force and moments of the DARPA snuff with bridge fairwater for straight-line motion.



LEGEND  
 □ - COMPUTED TOTAL FORCE  
 ○ - COMPUTED POTENTIAL FORCE  
 Δ - EXPERIMENTAL TOTAL FORCE

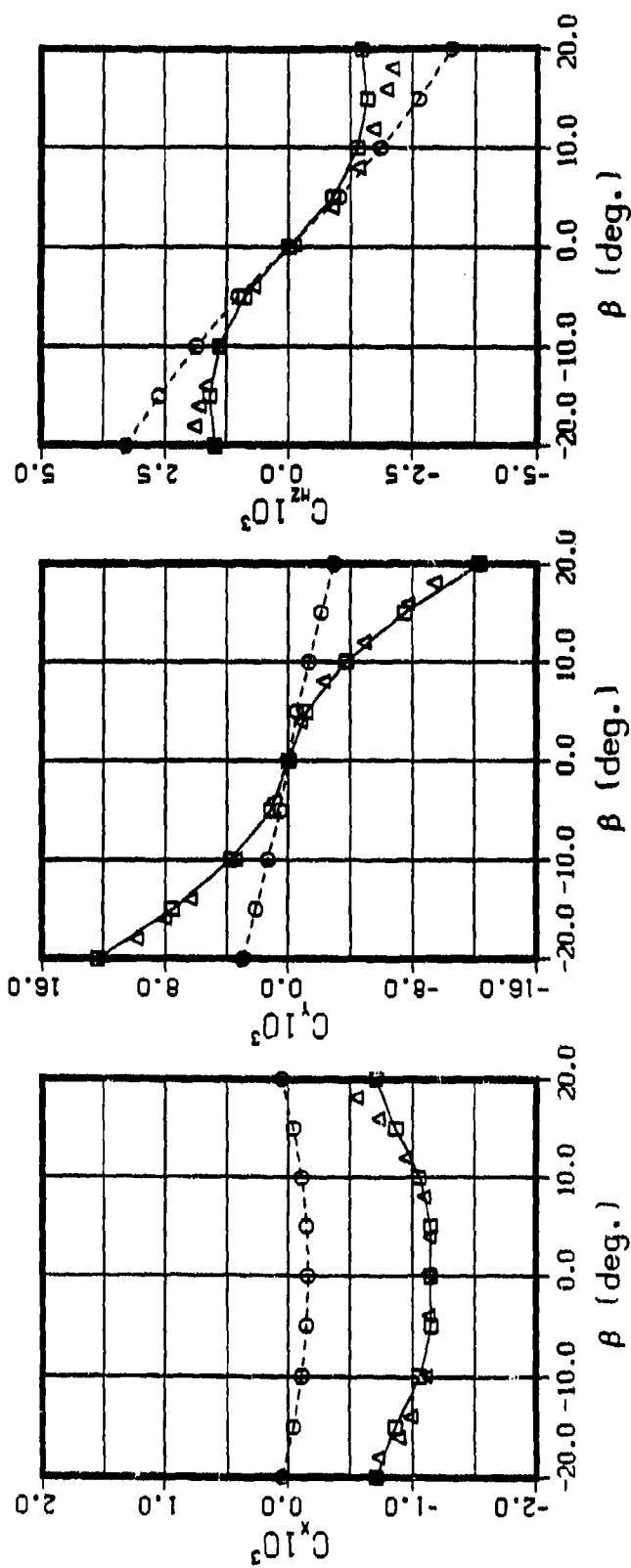


Fig. 20. Force and moments of the DARPA SUBOFF with stern appendages for straight-line motion

LEGEND  
 □ - COMPUTED TOTAL FORCE  
 ○ - COMPUTED POTENTIAL FORCE  
 Δ - EXPERIMENTAL TOTAL FORCE

(a)  $r' = 0.142$

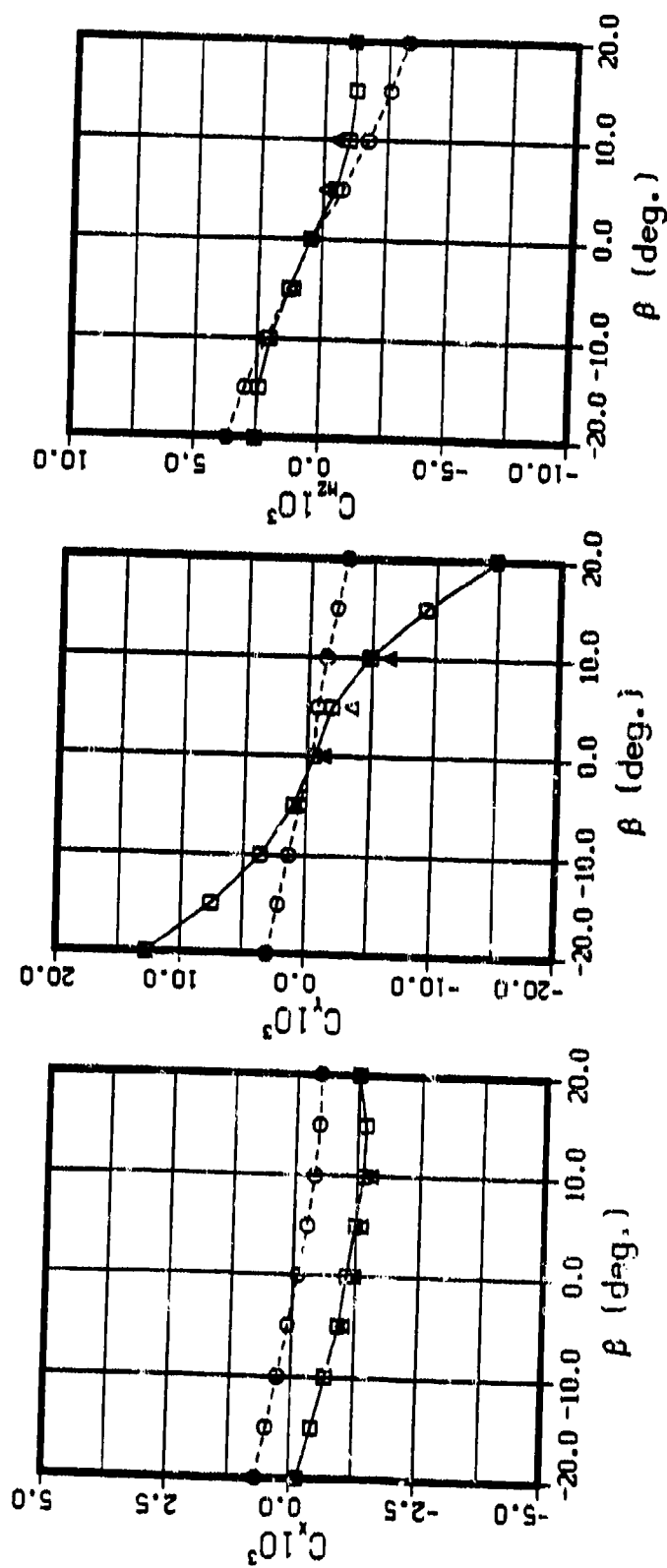


Fig. 21 - Forces and moments of Model 4621 with Appendix 2C for rotational motion

LEGEND  
 □ - COMPUTED TOTAL FORCE  
 ○ - COMPUTED POTENTIAL FORCE  
 Δ - EXPERIMENTAL TOTAL FORCE

(b)  $r' = 0.399$

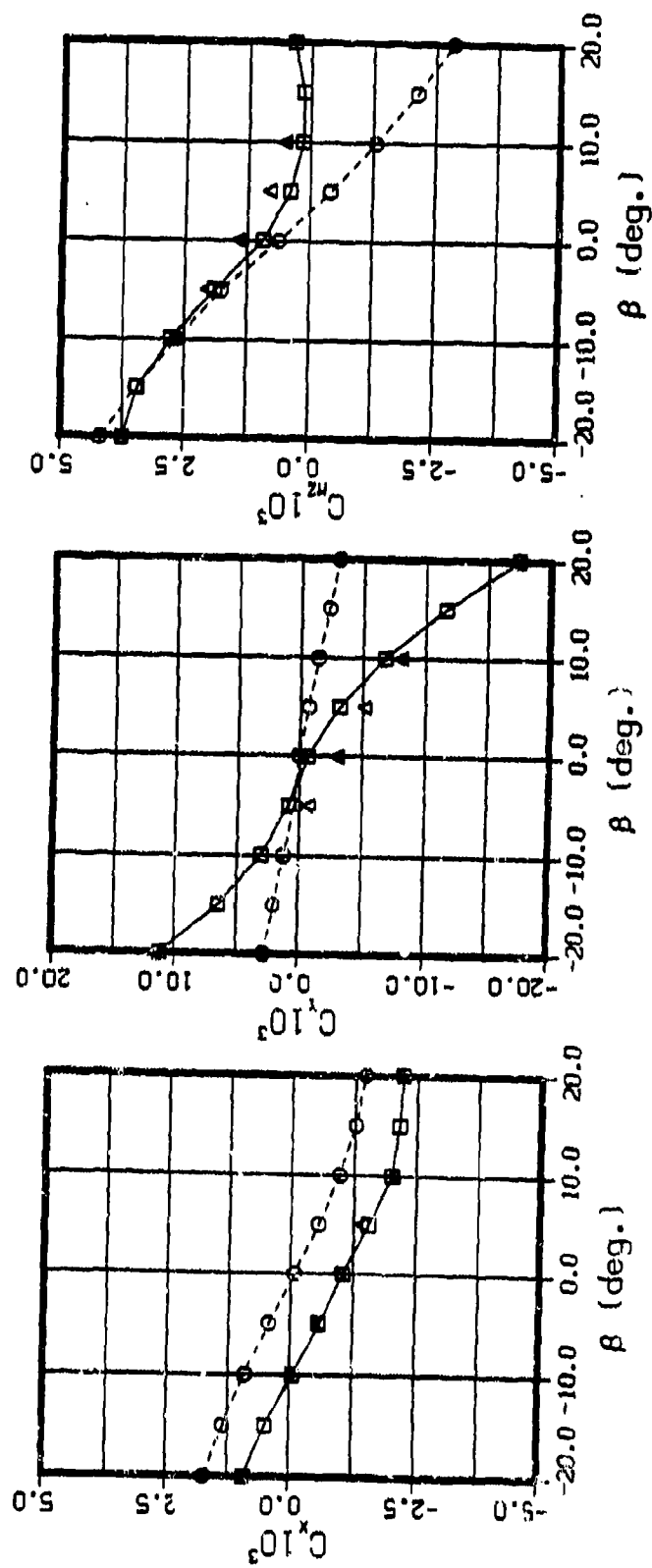


Fig. 21 - Continued

LEGEND  
 □ - COMPUTED TOTAL FORCE  
 ○ - COMPUTED POTENTIAL FORCE  
 Δ - EXPERIMENTAL TOTAL FORCE

(c)  $r' = 0.639$

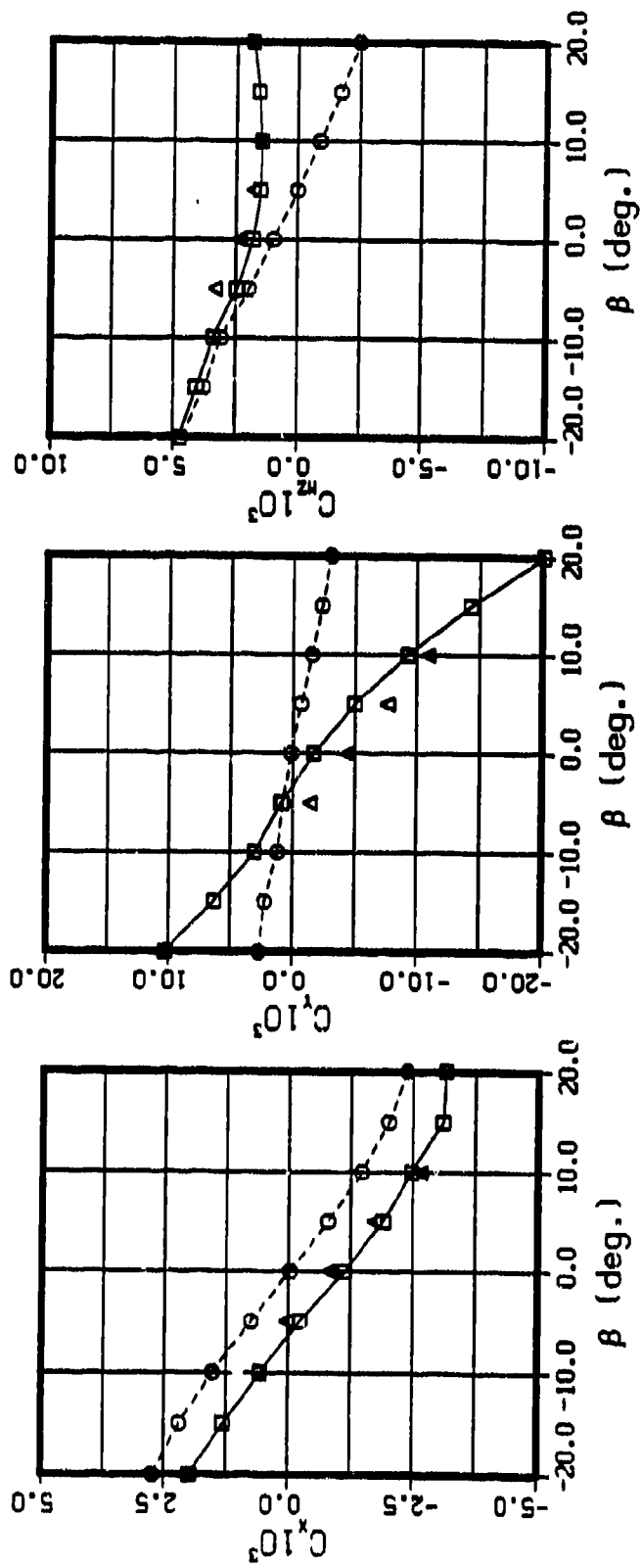


Fig. 21 - Continued

Table 1 - Geometric characteristics of sample models

Model name	Length (ft)	Beam (ft)	Length/Beam
Spheroid	6.56	1.64	4.00
Akron	19.62	3.32	5.91
4621	15.00	2.04	7.34
SUBOFF	14.29	1.67	8.57

Table 2 - Estimated errors in the numerical procedures performed for the Akron airship

(1) Angle of attack = 0 degrees

Force coeff.	Number of elements			
	280	364	420	476
$C_X$	$-0.189 \times 10^{-3}$	$-0.149 \times 10^{-3}$	$-0.129 \times 10^{-3}$	$-0.118 \times 10^{-3}$
$C_X / (C_X)_{280}$	1.0	0.80	0.68	0.62
$C_Z$	$0.165 \times 10^{-6}$	$0.194 \times 10^{-6}$	$0.162 \times 10^{-6}$	$0.188 \times 10^{-6}$
$C_Z / (C_Z)_{280}$	0	0	0	0

(2) Angle of attack = 21 degrees

$C_X$	$-0.121 \times 10^{-3}$	$-0.900 \times 10^{-4}$	$-0.745 \times 10^{-4}$	$-0.657 \times 10^{-4}$
$C_X / (C_X)_{280}$	1.0	0.74	0.62	0.54
$C_Z$	$-0.297 \times 10^{-3}$	$-0.223 \times 10^{-3}$	$-0.187 \times 10^{-3}$	$-0.164 \times 10^{-3}$
$C_Z / (C_Z)_{280}$	1.0	0.75	0.63	0.55

## REFERENCES

1. Hong, Y.S., "Forces and Moments Acting on a Submersible Moving Beneath the Free Surface or Near a Wall," David Taylor Research Center Report DTNSRDC/SHD-1233-01 (July 1987).
2. Hess, J.L. and A.M.O. Smith, "Calculation of Non-lifting Potential Flow about Arbitrary Three-dimensional Bodies," Douglas Aircraft Co., Inc., Report No. E.S. 4062 (March 1962).
3. Young, A.D., "The Calculation of the Total and Skin Friction Drags of Bodies of Revolution at Zero Incidence," Technical Report of the Aeronautical Research Committee R&M No. 1874 (1939).
4. Tomotika, S., "The Laminar Boundary Layer on the Surface of a Sphere in a Uniform Stream," Technical Report of the Aeronautical Research Committee R&M No. 1678, (1935).
5. Freeman, H.B., "Force Measurement on a 1/40-Scale Model of the U.S. Airship Akron," Report of National Advisory Committee for Aeronautics T.R. No. 432 (1932).
6. Cebeci, T. and A.M.O. Smith, "Analysis of Turbulent Boundary Layer," Academic Press, New York (1974).
7. Sivells, J.C. and R.H. Neely, "Method for Calculating Wing Characteristics by Lifting-line Theory Using Nonlinear Section Lift Data," National Advisory Committee for Aeronautics Report No. 865 (1947).
8. Kuethe, A.M. and C.Y. Chow, "Foundation of Aerodynamics: Bases of Aerodynamic Design," John Wiley & Sons, New York (1986).
9. Pitts, W.C., J.N. Nielsen, and G.E. Kaattari, "Lift and Center of Pressure of Wing-Body-Tail Combinations at Subsonic, Transonic, and Supersonic Speeds," National Advisory Committee for Aeronautics Report No. 1307 (1957).
10. Meier, H.U. and H-P. Kreplin, "Experimental Investigation of the Transition and Separation on a Body of Revolution," Second Symposium on Turbulent Shear Flow, July 2-4, 1979, London.
11. Gertler, M., "Resistance Experiments on a Systematic Series of Streamlined Bodies of Revolution - For Application to the Design of High-Speed Submarines," David Taylor Research Center Report C-297 (NS 715-080) (April 1950).
12. Jones, R., "The Distribution of Normal Pressures on a Prolate Spheroid," Technical Report of the Aeronautical Research Committee R&M 1061 (1925).
13. Dempsey, E.M., "Static Stability Characteristics of a Systematic Series of Stern Control Surfaces on a Body of Revolution," David Taylor Naval Ship Research and Development Center Report 77-0085 (August 1977).
14. Roddy, R., "Investigation of the Stability and Control Characteristics of Several Configurations of the DARPA SUBOFF Model (DTRC Model 5470) from Captive Model Experiments," David Taylor Research Center Report SHD-1298-08 (September 1990).
15. Whicker, L.F. and L.F. Fehlner, "Free-stream Characteristics of a Family of Low-Aspect-Ratio, All-Movable Control Surfaces for Application to Ship Design," David Taylor Model Basin Report 933 (December 1958).
16. Milne-Thomson, L.M., "Theoretical Hydrodynamics," London, MacMillan & Co Ltd. (1968).